

# Spurious Small-Scale Structure & Discreteness-Driven Relaxation in Cosmological Simulations

C. Power<sup>1\*</sup>, A. S. G. Robotham<sup>1</sup>, D. Obreschkow<sup>1</sup>, A. Hobbs<sup>2</sup> & G. F. Lewis<sup>3</sup>

<sup>1</sup>International Centre for Radio Astronomy Research, University of Western Australia, 35 Stirling Highway, Crawley, Western Australia 6009, Australia

<sup>2</sup>Institute for Astronomy, ETH Zurich, Wolfgang-Pauli-Strasse 27, CH-8093 Zurich, Switzerland

<sup>3</sup>Sydney Institute for Astronomy, School of Physics, A28, The University of Sydney, New South Wales 2006, Australia

arXiv:1606.02038v1 [astro-ph.CO] 7 Jun 2016

## ABSTRACT

There is strong evidence that cosmological  $N$ -body simulations dominated by Warm Dark Matter (WDM) contain spurious or unphysical haloes, most readily apparent as regularly spaced low-mass haloes strung along filaments. We show that spurious haloes are a feature of traditional  $N$ -body simulations of cosmological structure formation models, including WDM and Cold Dark Matter (CDM) models, in which gravitational collapse proceeds in an initially anisotropic fashion, and arises naturally as a consequence of discreteness-driven relaxation. We demonstrate this using controlled  $N$ -body simulations of plane-symmetric collapse and show that spurious haloes are seeded at shell crossing by localised velocity perturbations induced by the discrete nature of the density field, and that their characteristic separation should be approximately the mean inter-particle separation of the  $N$ -body simulation, which is fixed by the mass resolution within the volume. Using cosmological  $N$ -body simulations in which particles are split into two collisionless components of fixed mass ratio, we find that the spatial distribution of the two components show signatures of discreteness-driven relaxation in their spatial distribution on both large and small scales. Adopting a spline kernel gravitational softening that is of order the comoving mean inter-particle separation helps to suppress the effect of discreteness-driven relaxation, but cannot eliminate it completely. These results provide further motivation for recent developments of new algorithms, which include, for example, revisions of the traditional  $N$ -body approach by means of spatially adaptive anisotropic gravitational softenings or solve explicitly for the evolution of dark matter in phase space.

**Key words:** methods: numerical – galaxies: formation – galaxies: haloes – cosmology: theory – dark matter – large-scale structure of Universe

## 1 INTRODUCTION

Cosmological  $N$ -body simulations are a well established tool for studying the formation and non-linear evolution of structure in the Universe. Much of what we know about the Cold Dark Matter (CDM) model, the currently favoured theoretical framework within which we investigate the growth of this structure, derives from such simulations (e.g. Springel et al. 2006), and they have revealed that dark matter haloes have central densities that are divergent (e.g. Navarro et al. 2010); that the abundance of these haloes increases with decreasing halo mass  $M$  as  $M^{-\alpha}$  with  $\alpha \simeq 1.8$  (see Murray et al. 2013 for a survey of published halo mass functions); and that haloes contain a wealth of substructure, remnants of the merging hierarchy by which the halo assembled (e.g. Springel et al. 2008), independent of their mass (e.g. Ishiyama et al. 2013).

It can be argued that it is the abundance of small-scale structure – low-mass haloes and substructure haloes (hereafter subhaloes) – that is the defining prediction of the CDM model (e.g.

Power 2013), and so it is crucial that we understand its properties if we are to devise robust observational tests of the model. This can be appreciated by noting that alternatives to the CDM model modify its predictions on small scales. For example, self-interacting dark matter (SIDM) has a finite interaction cross section whose influence is greatest at high dark matter densities (e.g. Loeb & Weiner 2011), while Warm Dark Matter (hereafter WDM) free-streams in the early Universe to erase density perturbations that would otherwise collapse gravitationally to form low-mass haloes (e.g. Bode et al. 2001).

However, modelling structure formation in alternative dark matter models, especially those such as WDM in which initial small-scale density perturbations are suppressed, has proven challenging with the traditional  $N$ -body approach. Early WDM simulations (e.g. Bode et al. 2001; Knebe et al. 2002) appeared to confirm physical intuition that the abundance of low-mass haloes and subhaloes is suppressed relative to that in corresponding CDM simulations, but they also revealed the presence of ‘beads-on-a-string’, regularly spaced low-mass haloes along filaments (see rightmost panel of Figure 1). Initially it was argued that these haloes are the

\* chris.power@icrar.org

low-mass objects we might expect to form via fragmentation (e.g. Knebe et al. 2003), but subsequent work demonstrates that they are a numerical artifact (notably Wang & White 2007, but see also the more recent work of Myers et al. 2015, Sousbie & Colombi 2015, Hahn & Angulo 2016), with properties that are sensitive to the mass resolution of the  $N$ -body simulation – the inter-‘bead’ spacing decreases with decreasing particle mass as  $m_p^{1/3}$ , and the halo mass function rises rapidly at low masses below a mass scale that decreases with increasing mass resolution, again as  $m_p^{1/3}$  (cf. Wang & White 2007).

That such numerical artifacts arise is not surprising, as noted by e.g. Angulo et al. (2013a), Hahn et al. (2013), Myers et al. (2015), Sousbie & Colombi (2015), and Hahn & Angulo (2016). Traditional  $N$ -body simulations discretise the cosmic matter density field into particles, which, as noted by Binney (2004), introduces localised perturbations into the gravitational force a particle experiences along its trajectory over time. This implies that  $N$ -body particles are subject to velocity perturbations of magnitude,

$$\delta v \simeq \frac{Gm_p}{\epsilon v}; \quad (1)$$

here  $G$  is the gravitational constant,  $v$  is the typical peculiar velocity, which is fixed by the mass distribution, and  $\epsilon$  is the  $N$ -body particle’s gravitational softening length, which is usually chosen to be a fraction of the typical inter-particle separation within the simulation volume. The magnitude of these perturbations should remain small relative to the mean-field velocities induced by the large scale matter distribution if the evolution of the system is to be treated as collisionless.

In the case of the CDM model, velocity perturbations induced by discretisation are likely to be difficult to disentangle from velocities of a physical origin induced by the small-scale density perturbations encoded in the matter power spectrum. In contrast, these small-scale density perturbations are absent in WDM models below a particular mass scale, and gravitational collapse of lower mass objects is either suppressed or delayed relative to the CDM model; velocity perturbations induced by discretisation may be larger than the mean-field gravitational peculiar velocity, and so WDM models and generic dark matter models with reduced initial small-scale density perturbations should show evidence of these velocity perturbations, which trigger gravitational collapse and seed the formation of spurious haloes. We refer to the influence of these discreteness-induced velocity perturbations on the evolution of  $N$ -body particle trajectories as discreteness-driven relaxation.

Figure 1 shows ‘beads-on-a-string’ identified at  $z=0$  in a WDM  $N$ -body simulation that are likely are the product of discreteness-driven relaxation – they can be traced back to a Lagrangian region in the initial conditions that is planar, distinctly different from the regions that collapse to form physical haloes. This suggests that spurious haloes could be tagged by inspection of the initial conditions, and it has motivated efforts to ‘clean’ WDM simulations of spurious haloes (e.g. Lovell et al. 2014; Schneider et al. 2013). However, spurious haloes are likely to be a generic problem in cosmological  $N$ -body simulations, for the reasons outlined above, and so cleaning in this fashion will only pick out the most obvious instances (a similar point is made in Hahn & Angulo 2016). Indeed, as Ludlow & Porciani (2011) have noted, identifying the progenitors of low-mass haloes in the linear CDM density field remains an unsolved problem, which suggests strongly that a fraction of low-mass CDM haloes are possibly spurious, broken and scattered beads-on-a-string.

A number of studies have explored how discreteness effects

influences the accuracy of  $N$ -body simulations (e.g. Melott et al. 1997; Splinter et al. 1998; Knebe et al. 2000; Power et al. 2003; Binney & Knebe 2002; Diemand et al. 2004; Heitmann et al. 2005; Romeo et al. 2008), as well as hydrodynamical/ $N$ -body simulations (e.g. Angulo et al. 2013a); here the focus is on, in general, measurements of the power spectrum, correlation function, and the internal structure of dark matter haloes. This study focuses on the role discreteness plays in the formation of ‘beads-on-a-string’ that are so evident in WDM simulations; we demonstrate that discreteness-driven relaxation will arise naturally when a discretised density field is used to model the initially anisotropic phase of gravitational collapse (e.g. Zel’dovich 1970; Kuhlm, Melott, & Shandarin 1996) that is characteristic of realistic cosmological models; we highlight that it affects CDM simulations, although less readily apparent than in WDM simulations; and we show that traditional  $N$ -body methods can suppress discreteness-driven relaxation through appropriate choice of gravitational softening, but cannot fully eliminate it. As such, this study provides additional motivation for innovative new extensions to  $N$ -body algorithms that have been developed, such as those that solve for the evolution of dark matter by tracking phase space elements (e.g. Hahn et al. 2013; Hahn & Angulo 2016) or by incorporating gravitational softening that is both spatially adaptive and anisotropic (cf. Hobbs et al. 2015).

In the remainder of this paper, we undertake a series of numerical experiments, described in §2, to highlight the influence of discreteness-driven relaxation in  $N$ -body simulations of cosmological structure formation. To develop insights into how anisotropic gravitational collapse might seed the formation of spurious haloes, we simulate plane-symmetric collapse (cf. Zel’dovich 1970; Shandarin & Zeldovich 1989) in §3.1, which approximates how the initial collapse proceeds, and follow its spatial and phase space structure, varying the mass resolution ( $m_p$ ) and the gravitational softening ( $\epsilon$ ), both of which influence the magnitude of velocity perturbations (Eq 1), to identify when and where relaxation becomes important. Applying these insights to cosmological  $N$ -body simulations, in §3.2 we consider CDM and WDM models in which the collisionless component is split into two components; this approach is inspired by the numerical experiments of Binney & Knebe (2002), who looked for the signature of two-body relaxation via mass segregation on the internal structure of dark matter haloes. We investigate the degree to which the choice of gravitational softening ( $\epsilon$ ) can help to reduce discreteness-driven relaxation by examining the spatial structure of the dark matter and halo density fields, the mass functions of haloes, and the effects of mass segregation within haloes. Finally, in §4 we summarise our results, assessing the extent to which cosmological  $N$ -body simulations are impacted by discreteness-driven relaxation, and highlighting why novel extensions to the  $N$ -body are needed.

## 2 THE SIMULATIONS

**Plane-Symmetric Collapse Simulations** have an exact solution up to shell crossing (cf. Zel’dovich 1970; Shandarin & Zeldovich 1989) and provide a convenient approximation to the initially anisotropic phase of gravitational collapse that occurs in realistic dark matter models (i.e. CDM or models in which the CDM power spectrum is suppressed on small spatial scales). These runs will demonstrate that beads-on-a-string arise naturally when the gravitational softening  $\epsilon$  is smaller than the mean inter-particle separation  $\bar{d}$ , and that beading will occur on the scale of the mean inter-particle separation, which scales with the particle mass as

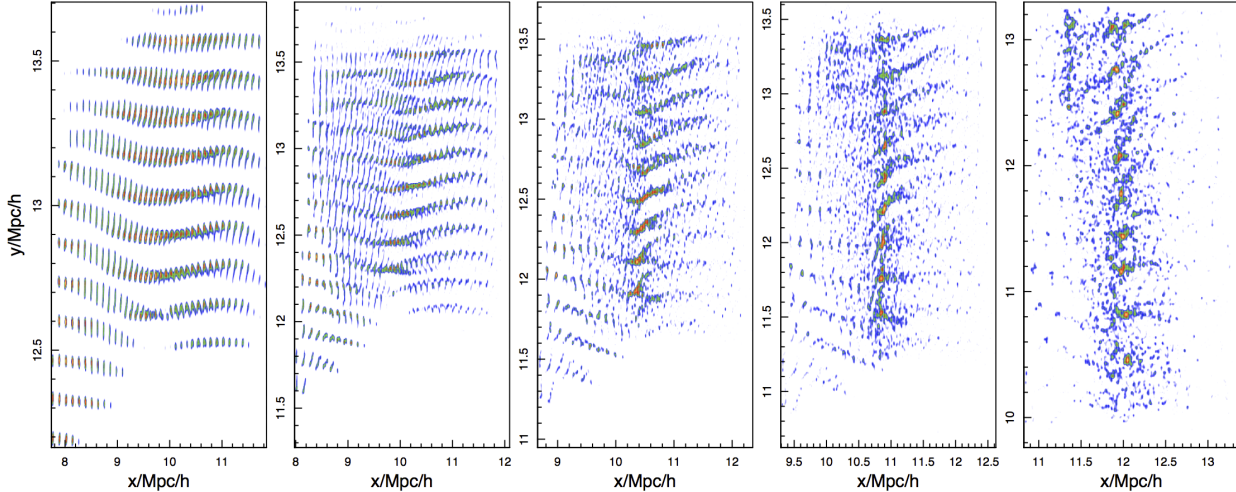


**Figure 1. “Beads-on-a-String” in simulations of the WDM model.** From left to right: In the rightmost panel we show an  $x$ - $y$  projection of beads-on-a-string, identified in a friends-of-friends catalogue at  $z=0$ , in a  $N$ -body simulation of a  $0.5 \text{ keV}/c^2$  WDM model.  $N$ -body particles are smoothed using a binned 2D kernel density estimate and coloured according to projected density. We track this material from  $z=0$  back to  $z=20$  (leftmost panel) to show that individual knots at late times grew from sheets at early times. This kind of procedure has been used to ‘clean’ WDM simulations of beads (e.g. Lovell et al. 2014).

$\bar{d} = (m_p/\Omega_0 \bar{\rho})^{1/3} = (V/N)^{1/3}$ , where  $\Omega_0$  is the matter density parameter,  $\bar{\rho}$  is the mean density,  $V$  is the simulation volume, and  $N$  is the number of particles in the simulation volume.

For our simulation set-up, we follow Hahn et al. (2013) in adopting an Einstein de Sitter cosmology ( $\Omega_0=1$ ,  $\Omega_\Lambda=0$ ) with a dimensionless Hubble parameter of  $h=0.7$ , a periodic box of side  $L_{\text{box}} = 10h^{-1}\text{Mpc}$  and a starting redshift of  $z_{\text{start}} = 99$ ; we performed runs with  $64^3$ ,  $128^3$  and  $256^3$  particles. The uniform particle distribution is a cubic mesh and we apply a one-dimensional sinusoidal potential perturbation  $\phi(\vec{x})$  along the  $x$ -axis, where

$$\phi(\vec{x}) = \phi_0 \cos(k_x x) \quad (2)$$

where  $\vec{x} = (x, y, z)$  and  $k_x = 2\pi/L_{\text{box}}$ . We choose the amplitude of the potential perturbation  $\phi_0$  such that shell crossing occurs at  $z=4$ . Particle positions and velocities are initialised by applying the Zel'dovich (1970) approximation. In a subset of the runs, we split the particles into two components with varying mass ratios; see below for further details.

**Two Component Cosmological  $N$ -body Simulations** allow us to assess the effects of discreteness-driven relaxation by looking at differences in the spatial distribution of two collisionless components of fixed mass ratio that have co-evolved in the same gravitational potential. To do this, we consider a CDM model and a WDM counterpart (we have runs with  $m_{\text{WDM}} = (0.2, 0.5)\text{keV}/c^2$  but concentrate on the  $0.2\text{keV}/c^2$  runs to simplify our analysis) using boxes of side  $L_{\text{box}} = 20h^{-1}\text{Mpc}$  with starting redshift  $z_{\text{start}} = 99$  and assuming cosmological parameters of  $\Omega_0 = 0.27$ ,  $\Omega_\Lambda = 0.73$ ,  $h = 0.705$  and  $\sigma_8 = 0.81$  at  $z = 0$  (Komatsu et al. 2011). For our two collisionless components, we consider mass ratios of  $1/\sqrt{2}$  and  $1/4$  respectively. These runs were initialised from a regular cubic mesh and the lighter components was offset by  $\bar{d}/2$  in each of the three dimensions. The fiducial runs consist of  $2 \times 256^3$  particles, but we also have lower resolution runs of  $2 \times 64^3$  particles for comparison with the results of Binney & Knebe (2002).

Initial conditions were created using standard techniques (e.g. Power et al. 2003) – a statistical realization of a Gaussian random

density field is generated in Fourier space, with variance given by the linear matter power spectrum, and the Zel'dovich approximation is used to compute initial particle positions and velocities. The power spectrum for the CDM model is obtained by convolving the primordial power spectrum  $P(k) \propto k^{n_{\text{spec}}}$  with the transfer function appropriate for our chosen set of cosmological parameters, computed using the Boltzmann code CAMB (cf. Lewis et al. 2000). Following Bode et al. (2001), we obtain the initial power spectra for our WDM models by filtering the CDM power spectrum with an additional transfer function of the form

$$T^{\text{WDM}}(k) = \left( \frac{P^{\text{WDM}}(k)}{P^{\text{CDM}}(k)} \right)^{1/2} = [1 + (\alpha k)^{2\nu}]^{-5/\nu} \quad (3)$$

where  $k$  is the wave-number;  $\nu=1.2$  is a numerical constant; and  $\alpha$  is a function of the WDM particle mass (see equation A9 of Bode et al. 2001), which we write as

$$\alpha = 0.0413 \left( \frac{\Omega_X}{0.27} \right)^{0.15} \left( \frac{h}{0.705} \right)^{1.3} \left( \frac{m_X}{\text{keV}/c^2} \right)^{-1.15} \left( \frac{g_X}{1.5} \right)^{0.29}. \quad (4)$$

Here it is assumed that the WDM particle is the thermal relic  $X$  with mass  $m_X$ ;  $\Omega_X$  is the global matter density parameter of  $X$ ; and  $g_X$  is the number of spin degrees of freedom, assumed to be 1.5 for WDM (cf. Bode et al. 2001). For reference, we follow convention and define a half-mode length  $\lambda^{\text{half}}$ , as the point at which the WDM transfer function drops to 1/2 (see, e.g., Schneider et al. 2012); in this case,

$$k^{\text{half}} = \frac{2\pi}{\lambda^{\text{half}}} = \frac{1}{\alpha} \left( 2^{\mu/5} - 1 \right)^{1/2\mu} \quad (5)$$

and so the equivalent half-mode mass is,

$$M_{\text{WDM}}^{\text{half}} = \frac{4\pi}{3} \bar{\rho} \left( \frac{\lambda^{\text{half}}}{2} \right)^3 = \frac{4\pi}{3} \bar{\rho} \left[ \pi \alpha \left( 2^{\mu/5} - 1 \right)^{-1/2\mu} \right]^3. \quad (6)$$

The corresponding values for the  $m_{\text{WDM}}=(0.2, 0.5)\text{keV}/c^2$  models are  $M_{\text{WDM}}^{\text{half}} \simeq (149.8, 6.3) \times 10^{10} h^{-1} M_\odot$ .

Note that we do not include an additional velocity to mimic

the effects of free-streaming in the early Universe<sup>1</sup>; this is possibly an important omission for the  $0.2 \text{ keV}/c^2$  run, less so for the  $0.5 \text{ keV}/c^2$  run (e.g. Colín et al. 2008; Angulo et al. 2013b), but we note that modelling this effect correctly in a  $N$ -body simulation is difficult – it can lead to an unphysical excess of small-scale power in the initial conditions if the simulation is started too early (see Figure 1 of Colín et al. 2008 for a nice illustration of this problem) – so for clarity we ignore this effect (see also discussion in Power 2013).

**Simulation Parameters** All simulations were run using the parallel TreePM code GADGET2 (Springel 2005). We use the spline kernel gravitational softening with a comoving softening scale  $\epsilon$  (cf. Eq 4 of Springel 2005), such that the density distribution of a single particle is a convolution of a Dirac  $\delta$ -function and a normalised kernel and is expressed as  $\tilde{\delta}(\mathbf{x}) = W(|\mathbf{x}|, 2.8\epsilon)$ ; here the spline kernel  $W(r)$  is written as

$$W(r, h) = \frac{8}{\pi h^3} \begin{cases} 1 - 6(r/h)^2 + 6(r/h)^3, & 0 \leq r/h \leq \frac{1}{2} \\ 2(1 - r/h)^3, & \frac{1}{2} \leq r/h \leq 1 \\ 0, & r/h > 1. \end{cases} \quad (7)$$

We keep the softening scale  $\epsilon$  fixed in comoving coordinates, and use individual and adaptive timesteps for each particle,  $\Delta t = \eta\sqrt{\epsilon/a}$ , where  $a$  is the magnitude of a particle's gravitational acceleration and  $\eta = 0.05$  determines the accuracy of the time integration. We used GADGET in standard TreePM mode with a PM dimension of 512. For our reference softening, we define  $\epsilon_0 = \bar{d}$  and we considered values of  $\epsilon = (0.01, 0.1, 1, 10)\epsilon_0$ . We considered cases in which the softening was fixed in physical units and in which the time integration accuracy was made more stringent, but these did not affect our general findings. For completeness, we have tested the sensitivity of our results to the underlying TreePM algorithm by running versions of our simulations with gravitational forces computed both in purely tree mode (i.e. with the -DPMGRID flag switched off when compiling GADGET2 and in TreePM mode (i.e. with -DPMGRID switched on) with a PM grid dimension that varies between 64 and 1024 by factors of 2. Full details of these tests are presented in the appendix.

**Halo Identification** We use the SubFind algorithm of Springel et al. (2001) to generate friends-of-friends (FOF) catalogues, assuming a linking length of  $b=0.2\bar{d}$ . For each FOF group we determine its centre-of-density  $\vec{r}_{\text{cen}}$  using the iterative “shrinking spheres” algorithm and identify this as the halo centre (cf. Power et al. 2003). From this, we calculate quantities such as virial radius  $r_{\text{vir}}$ , which we define as the radius at which the mean interior density is  $\Delta_{\text{vir}} = 200$  times the critical density of the Universe at that redshift,  $\rho_c(z) = 3H^2(z)/8\pi G$ , where  $H(z)$  and  $G$  are the Hubble parameter at  $z$  and the gravitational constant respectively. The corresponding virial mass  $M_{\text{vir}}$  is

$$M_{\text{vir}} = \frac{4\pi}{3} \Delta_{\text{vir}} \rho_c r_{\text{vir}}^3. \quad (8)$$

<sup>1</sup> In practice this is done by assigning a random velocity component (typically drawn from a Fermi-Dirac distribution) to particles in addition to their velocities predicted by linear theory (cf. Klypin et al. 1993; Colín et al. 2008; Maccio et al. 2012)

## 3 RESULTS

### 3.1 Plane-Symmetric Collapse

**Phase Space Structure:** In Figure 2 we show slices through phase space of the one-dimensional wave (peculiar velocity  $v_x$  versus comoving position  $x$ ) at approximately shell crossing ( $z \simeq 4$ , upper panels) and at late times ( $z \simeq 0$ , lower panels). Here we have varied systematically the gravitational comoving softening, adopting values of (from left to right)  $\epsilon/\epsilon_0 = (1, 0.1, 0.01)$  in the  $256^3$  run. What is striking in this Figure is the impact that  $\epsilon$  has on the phase space structure of the wave. At early times, prior to shell crossing, the difference in the evolution of the waves in the different runs is negligible. It is at shell crossing that differences in evolution start to become apparent – the smaller the value of  $\epsilon$ , the more pronounced the deviation from the predicted evolution. Rather than evolving as a thin sheet that preserves its structure as it winds up (as in the cases when  $\epsilon = \epsilon_0$ ), the sheet thickens at shell crossing, arising from velocity perturbations that grow with decreasing  $\epsilon$  as  $\epsilon^{-1}$  (cf. Eq 1) and which fragment into clumpy structures in phase space at later times (cf. lower-middle and lower-right panels).

**Spatial Structure:** In Figure 3 we show the resulting projected spatial distribution ( $x$  versus  $y$ ) of particles at  $z=0$  within the region where the density enhancement is greatest in the  $64^3$ ,  $128^3$  and  $256^3$  runs (left to right columns) for adopted softening of  $\epsilon/\epsilon_0=1$  (top row) and  $0.01$  (bottom row). The smaller value of  $\epsilon$  is a little more conservative than is usually adopted in large uniform resolution  $N$ -body simulations (a factor of 3–5 smaller), but it highlights the point that we wish to make. We expect particles to oscillate collisionlessly about the midplane ( $x=5h^{-1}\text{Mpc}$ ); this is what we observe in the regularity of the  $\epsilon=\epsilon_0$  case, with particle density varying smoothly along their trajectory. This regularity breaks down as  $\epsilon$  is reduced and distinct clumps have formed in the midplane, which are spaced at roughly the mean inter-particle separation of the simulation. This is what we would expect based on the behaviour evident in Figure 2 – if  $\epsilon$  is too small,  $N$ -body particles are subject to large velocity perturbations in what would otherwise be the smooth gravitational field in which they move because of close encounters with other  $N$ -body particles. These perturbations act to scatter particle momenta, diffusing the initial planes away and producing the clumps evident in the midplane in the lower panels columns of Figure 3.

**Two-Component Pancakes:** To verify behaviour we see in the cosmological simulations present in § 3.2, we have also run two collisionless components versions of these experiments, looking at mass ratios of  $(1/1, 1/\sqrt{2}, 1/4, 1/10)$  and softenings of  $\epsilon/\epsilon_0=(1, 0.1, 0.01)$ . The results are consistent with those already presented – we see systematic deviations from the expected evolution for softenings  $\epsilon \ll \epsilon_0$  and these are seeded at shell crossing. As highlighted by Figure 4, which shows the phase space structure in these two-component pancakes at approximate shell crossing ( $z_c \simeq 4$ ), that the larger the mass ratio, the larger the initial momentum perturbation experienced by the less massive collisionless component (filled circles), and as the system evolves post-shell crossing, the more the two components mix in the area of overlap (see Figure 5).

We note at this point that these trends are consistent with behaviour reported by Angulo et al. (2013a), who found evidence for spurious coupling between baryon and dark matter components in their cosmological simulations – where the two components have a mass ratio of  $\sim 1/6$ . They argued that this arises from a loss of collisionality that arises from discretization of the density field and the

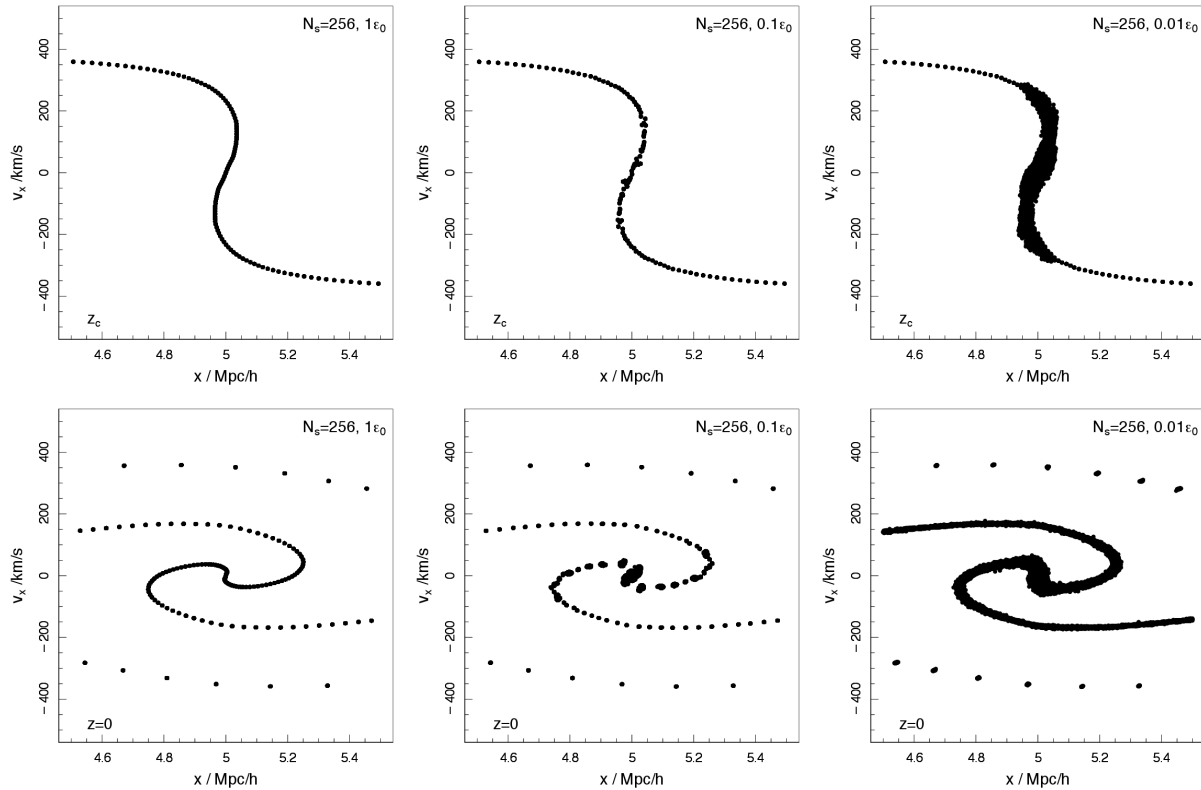


**Figure 2. Plane-Symmetric Collapse: Phase Space Structure.** Here we show the phase space structure in the  $256^3$  run, at approximately shell crossing ( $z=4$ ; upper panels) and at late times ( $z=0$ ; lower panels). Here  $v_x$  is the peculiar velocity along the  $x$ -direction and  $x$  is the comoving position. The gravitational softening  $\epsilon$  decreases by factors of 10 from  $\epsilon_0$  (left-most panel) to  $0.01 \epsilon_0$  (right-most panel).

use of high force resolution (i.e.  $\epsilon \ll \epsilon_0$ ), and can be overcome by having ‘softer’ gravitational forces on scales below the mean inter-particle separation, to suppress spurious coupling between baryons and dark matter. We return to this point below.

### 3.2 Cosmological Simulations

To assess how discreteness-driven relaxation of the form just described affects cosmological  $N$ -body simulations, we follow Binney & Knebe (2002, hereafter BK02) and use two sets of collisionless particles to represent the dark matter distribution. BK02 were interested in identifying the influence of two-body relaxation on the internal structure of dark matter haloes by looking for evidence of mass segregation, with the more massive component’s particles preferentially occupying the inner parts of haloes. Here we are interested in how more and less massive (hereafter heavier and lighter)  $N$ -body particles cluster, with the expectation that differences should be negligible if discreteness effects are unimportant. In what follows, we show results for the runs in which the mass ratio is 1/4, but have also checked for consistency in trends present in the runs with a mass ratio of  $1/\sqrt{2}$ . We also distinguish between FOF groups, overdensities recovered by the algorithm in the dark matter density field that can be either physical or spurious, rather than haloes, the subset of FOF groups that correspond to physical overdensities.

**Spatial Distribution:** In Figures 6 and 7 we show the  $z=0$  projected dark matter density distribution (upper panels) and the locations of the centres of FOF groups with  $N_{\text{FOF}} \geq 30$  par-

ticles (lower panels) within a  $2 h^{-1}$  Mpc slice in the CDM and WDM runs (lower panels), evolved with (from left to right)  $\epsilon/\epsilon_0=(0.01, 0.1, 1)$ ; the colour bar indicates logarithm of projected  $N$ -body particle/FOF group number density. These Figures show that the properties of the large-scale structure – its topology, the locations of massive groups, and the density contrast within the dominant filaments – are consistent between CDM and WDM runs and between runs with different softenings, and the deficit in the abundance of small-scale structure in the WDM runs with respect to the corresponding CDM run is also readily apparent.

However, they also reveal some interesting differences in the influence of  $\epsilon$  on the structure of filaments and the distribution of FOF groups between the CDM and WDM runs. In the WDM runs, varying  $\epsilon/\epsilon_0$  between 0.01 to 1 has a relatively small impact on either large-scale filamentary structure or the spatial distribution of groups – filaments delineated by groups are readily identifiable in all of the runs. The projected dark matter density within filaments in the  $\epsilon/\epsilon_0=1$  run is smoother than in the  $\epsilon/\epsilon_0 < 1$  runs, although the projected FOF group distribution reveals the presence of low-mass groups. Small differences are evident in the low-density regions in the projected distribution of FOF groups, where the artifact of the initial particle grid has been picked up by the FOF algorithm, most noticeably in the  $\epsilon/\epsilon_0=1$  case centred on  $(x, y) \simeq (6, 8) h^{-1} \text{Mpc}$ . In contrast, the impact of  $\epsilon$  is more marked in the CDM runs than in the WDM runs, with the key differences being between the  $\epsilon/\epsilon_0 < 1$  and  $\epsilon/\epsilon_0=1$  cases. Contrasting these two cases and focusing on the projected dark matter density maps, we see that minor filaments are smooth and continuous when  $\epsilon/\epsilon_0=1$  whereas they are fragmented and clumpy when  $\epsilon/\epsilon_0 < 1$ , while low density regions con-

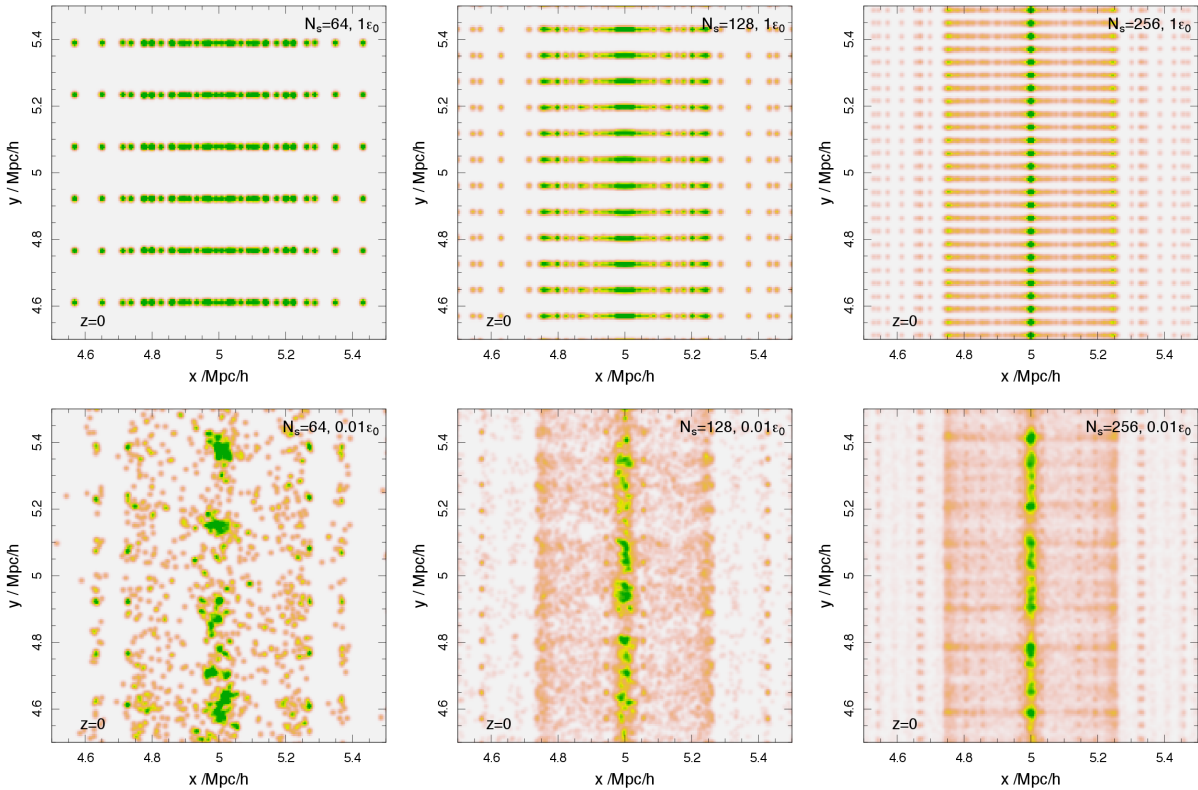


**Figure 3. Plane-Symmetric Collapse: Spatial Structure.** Here we show the projected spatial distribution (in the  $x$ - $y$  plane) at late times ( $z=0$ ) in the  $64^3$ ,  $128^3$  and  $256^3$  runs (left to right) with gravitational softening lengths  $\epsilon = 0.01 \epsilon_0$ , where  $\epsilon_0 = \bar{d}$ .

tain fewer structures when  $\epsilon/\epsilon_0=1$  compared to the  $\epsilon/\epsilon_0 < 1$  case. The projected FOF group distribution reveals a fog of low-mass groups filling the simulation volume when  $\epsilon/\epsilon_0 < 1$ , whereas this fog is suppressed when  $\epsilon/\epsilon_0=1$ ; the density of lower-mass groups in the environs of the most massive groups within the simulation volume is similar for all values of  $\epsilon$ .

We quantify these visual impressions in Figures 8 and 9, where we make explicit how varying  $\epsilon$  in softening affects structure in the CDM and WDM runs. Figure 8 shows the differential mass functions measured in the CDM (red curves) and WDM (blue curves) runs for softenings of  $\epsilon/\epsilon_0=1$  (solid), 0.1 (dashed), and 0.01 (dotted), where masses correspond to  $M_{\text{FOF}}$  rather than  $M_{200}$ . For comparison, Sheth & Tormen (1999) mass functions estimated using the HMFCalc tool of Murray et al. (2013) for the appropriate cosmological dark matter model are shown as light curves. The vertical dashed line indicates the halo mass corresponding to  $r_{200} = \epsilon_0$ , i.e.  $M(\epsilon_0) = 4\pi/3 \times 200 \times \rho_{\text{crit}} \times \epsilon_0^3$ , which we might consider to be (approximately) the minimum halo mass in the  $\epsilon/\epsilon_0=1$  runs.

Choosing  $\epsilon/\epsilon_0=1$  suppresses the mass function for  $M_{\text{FOF}} \lesssim 10^{11} h^{-1} M_\odot$  in both CDM and WDM runs, but there is no sharp decline with decreasing mass in either case, as we might expect; indeed, the upturn in the mass function associated with WDM mass functions persists, albeit shifted to smaller masses by  $\sim 0.2$  dex. Choosing  $\epsilon/\epsilon_0=0.1$  or 0.01 makes little difference to either the shape or amplitude of the mass function. This persistence of the upturn in all of the WDM runs suggests that even softenings of  $\epsilon/\epsilon_0=1$ , while helping to suppress relaxation, cannot eliminate it in realistic circumstances, where initial collapse will seldom be symmetric. It also highlights the inherent difficulty in post-processing

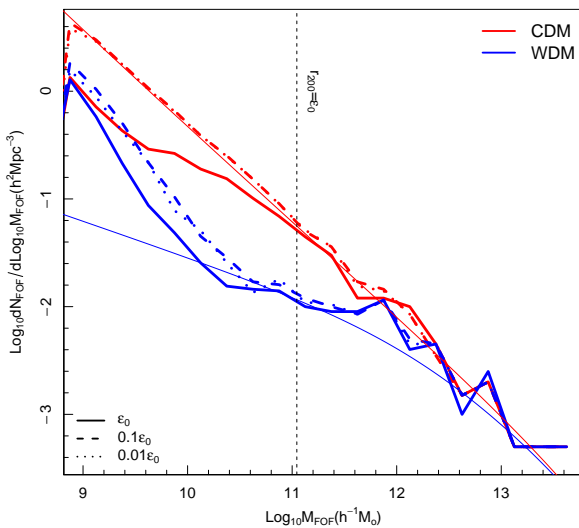


**Figure 8. FOF Group Mass Functions.** Here we show the differential mass functions of FOF groups (containing both components of particle) in the  $\epsilon/\epsilon_0=(1,0.1,0.01)$  runs (heavy solid, dashed, dotted); light solid curves indicate the appropriate CDM and WDM halo mass functions, computed using HMFCalc (Murray et al. 2013), while the vertical dashed line indicates the (approximate) minimum halo mass we might expect in the  $\epsilon/\epsilon_0=1$  run, where the halo virial radius  $r_{200}$  is set to  $\epsilon_0$ .

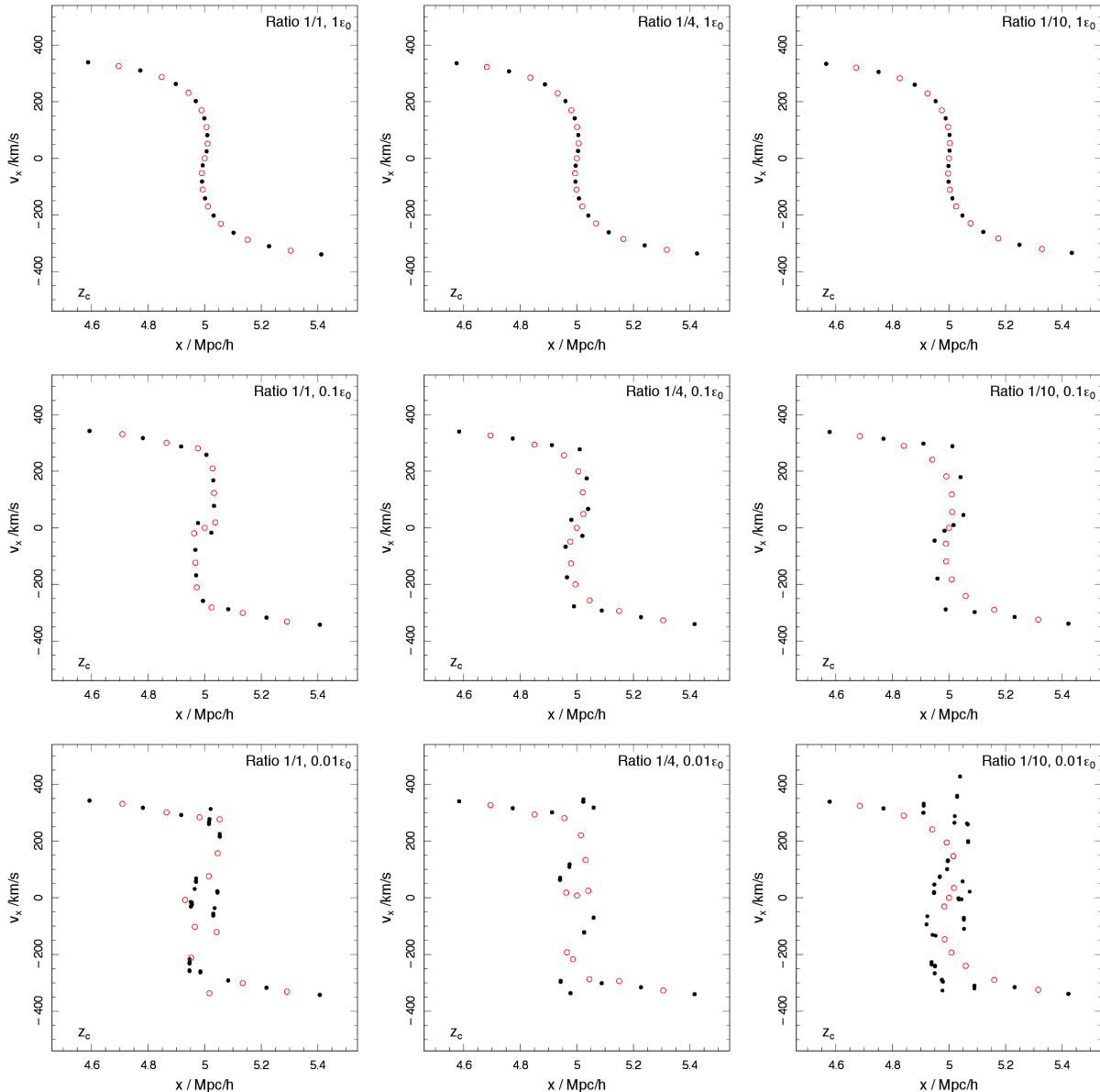


**Figure 4. Two-Component Plane-Symmetric Collapse: Phase Space Structure** In the upper, middle, and lower rows, we show the phase space structure at  $z_c \simeq 4$  in the  $\epsilon/\epsilon_0 = (0.01, 0.1, 1)$  runs, where the ratio of particle masses varies from 1/1 (left column) to 1/4 (middle column) to 1/10 (right column). Filled (open) circles correspond to the less (more) massive component.

halo catalogues to remove spurious haloes – even in the most conservative limit of  $\epsilon/\epsilon_0=1$ , evidence for numerical artifacts persists.

In Figure 9, we compare and contrast the  $\epsilon/\epsilon_0=0.01$  and 1 runs using difference maps (i.e. difference in pixel by pixel values of projected density maps). This confirms the impression from Figures 6 and 7 – that reducing the softening seeds the growth of small-scale structure in the density field in the CDM runs, whereas this is negligible in the WDM runs. This is the behaviour we would expect in the presence of discreteness-driven relaxation of the kind that we have described. Because there is power on all scales in the CDM model, gravitational collapse proceeds early – how early depends on the scales that are resolved in the  $N$ -body simulation. In our runs containing two collisionless components, the heavier particles seed local gravitational perturbations that act to modify the velocity distributions of particles; precisely how will depend

on the local gravitationally induced velocity field. The net effect, however, is to amplify density perturbations and to cause regions to undergo premature gravitational collapse<sup>2</sup>. The lack of power on small scales in the WDM runs delays gravitational collapse and so the effect of the localised gravitational and momentum perturbations introduced by the heavier particles is delayed; the main differences arise in the filaments, where the beading characteristic of spurious halo formation is evident.

In Figure 10, we investigate how the spatial distribution of the two components (i.e. heavy and light particles) compare in the  $\epsilon/\epsilon_0=0.01$  CDM and WDM runs by looking at difference maps of

<sup>2</sup> We see a similar effect in WDM simulations in which a thermal velocity component is added explicitly to dark matter particles in the initial conditions to mimic the effect of free-streaming(cf. §2.1.2. of Power 2013)

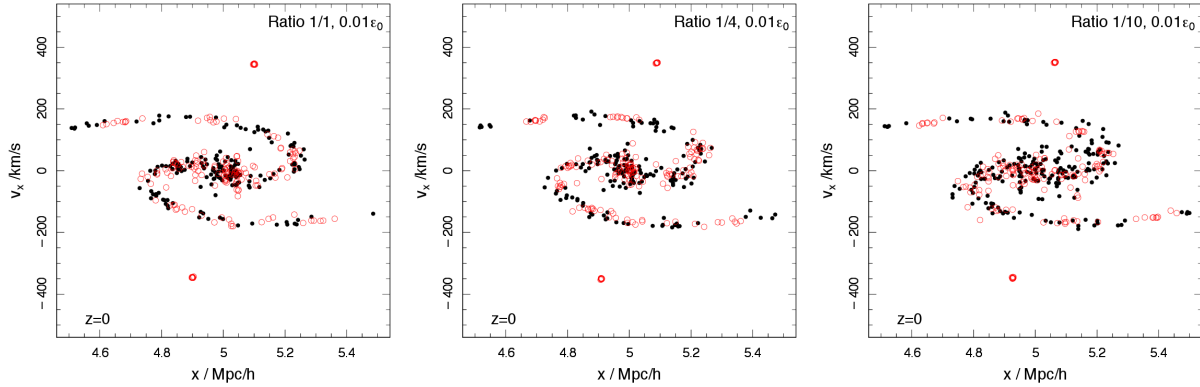


**Figure 5. Two-Component Plane-Symmetric Collapse: Phase Space Structure** Here we show the phase space structure at  $z=0$  in the  $\epsilon/\epsilon_0=0.01$  run, where the ratio of particle masses varies from 1/1 to 1/4 to 1/10 (left to right). Filled (open) circles correspond to the less (more) massive component.

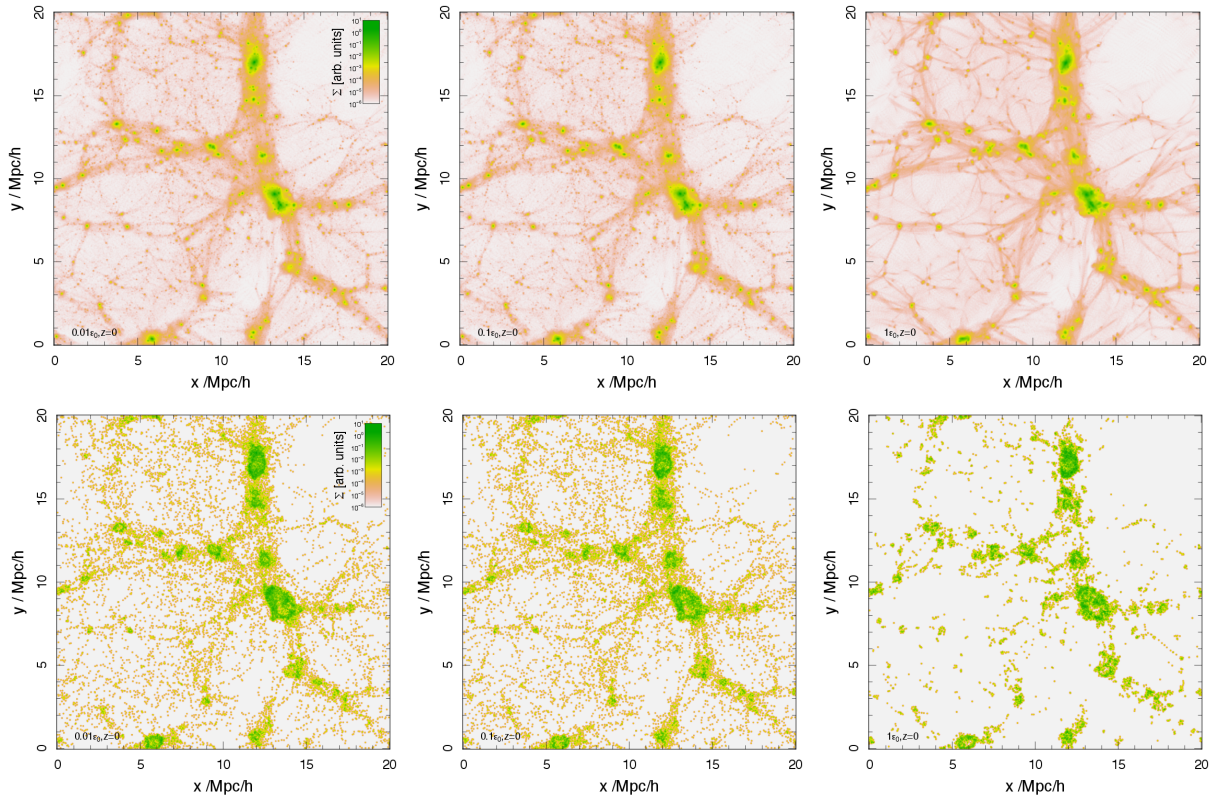


**Figure 6. Spatial Distribution of FOF Groups: CDM Case.** Upper Panels: The projected dark matter density distribution in the  $\epsilon/\epsilon_0=(0.01, 0.1, 1)$  runs. The colour bar indicates the projected density scale in arbitrary units; the same scale is used in each panel. Lower Panels: Spatial distribution of FOF group centres, where centre corresponds to centre of density  $\bar{r}_{\text{cen}}$ ; see text for further details.

projected densities within pixels. This reveals that the projected densities of the two components are similar within filaments and FOF groups in both CDM and WDM runs. We expect the components to be well mixed and to have similar projected densities within groups, where gravitational collapse is well into its non-linear phase. Within filaments, collapse is only mildly non-linear, and we might expect to see the components clearly separated in projected density (similar to Figure 3), as we see in the WDM run in the low density regions. The pattern of gravitational collapse is plainly much more complex in cosmological simulations than in the idealised plane-symmetric collapse simulations of § 3.1, and so

we might not expect such clear separation in projected densities of the components; however, the plane-symmetric collapse simulations with small softenings revealed that perturbations at shell crossing seed momentum perturbations, which act to smear out the separation between the initial planes of particles (and as the two components collapse runs also showed, separations between the components), and so we expect the components to be mixed within filaments too. Interestingly, in the WDM run, it is striking how the filaments, and consequently the areas where beading arising from spurious halo formation, run orthogonally to the delineation in mass; this is much more difficult to discern in the CDM

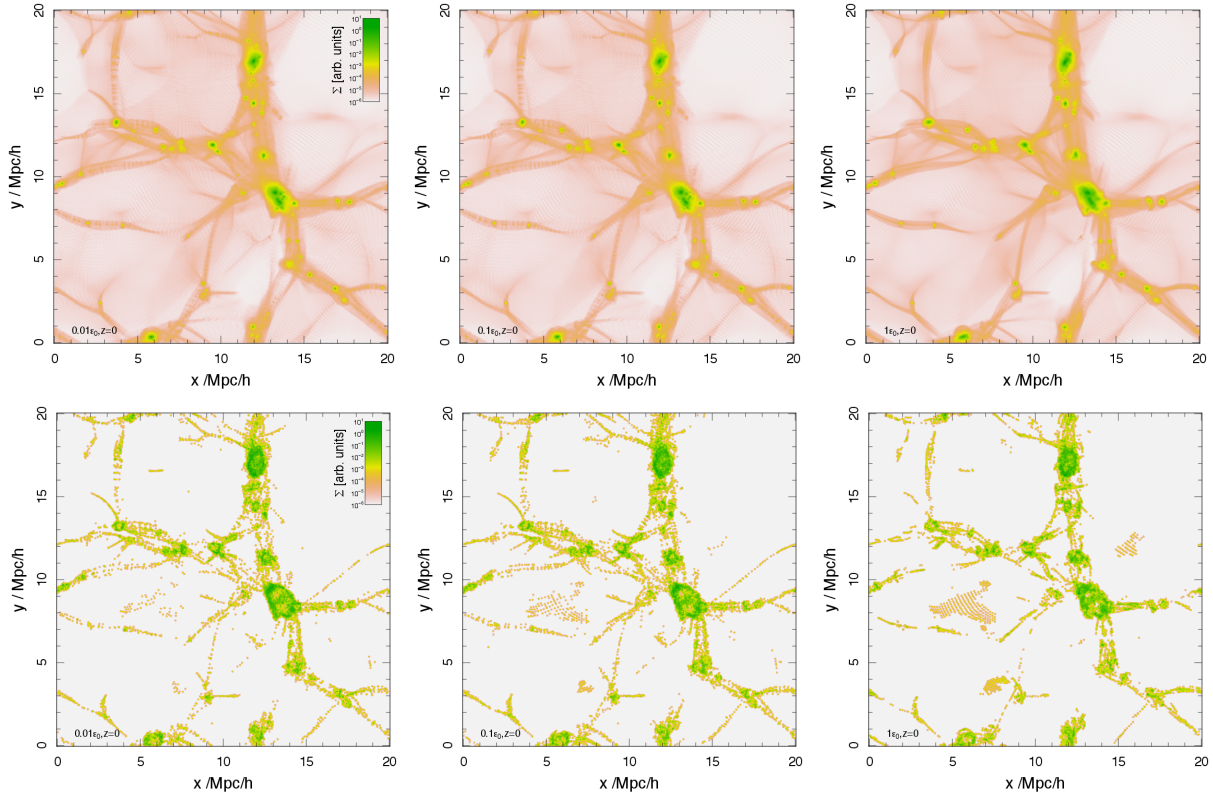


**Figure 7. Spatial Distribution of FOF Groups: WDM Case.** As in Figure 6, we show the projected dark matter density distribution in the  $\epsilon/\epsilon_0=(0.01,0.1,1)$  runs (upper panels) and the spatial distribution of FOF group centres (lower panels).

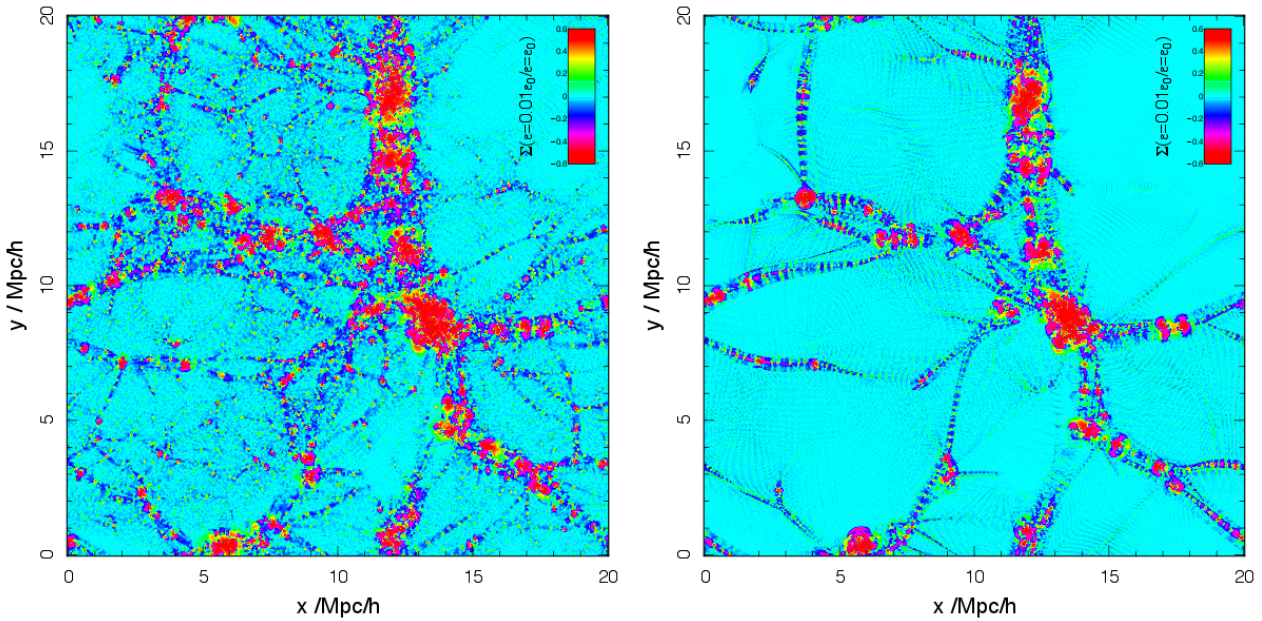


**Figure 9. Difference Maps: Delineating by Softening.** Here we show the difference in projected density distribution between the  $\epsilon=0.01\epsilon_0$  and  $\epsilon=\epsilon_0$  CDM and WDM runs (left and right panels respectively). We use the atan mapping in the R `magicaxis` package.

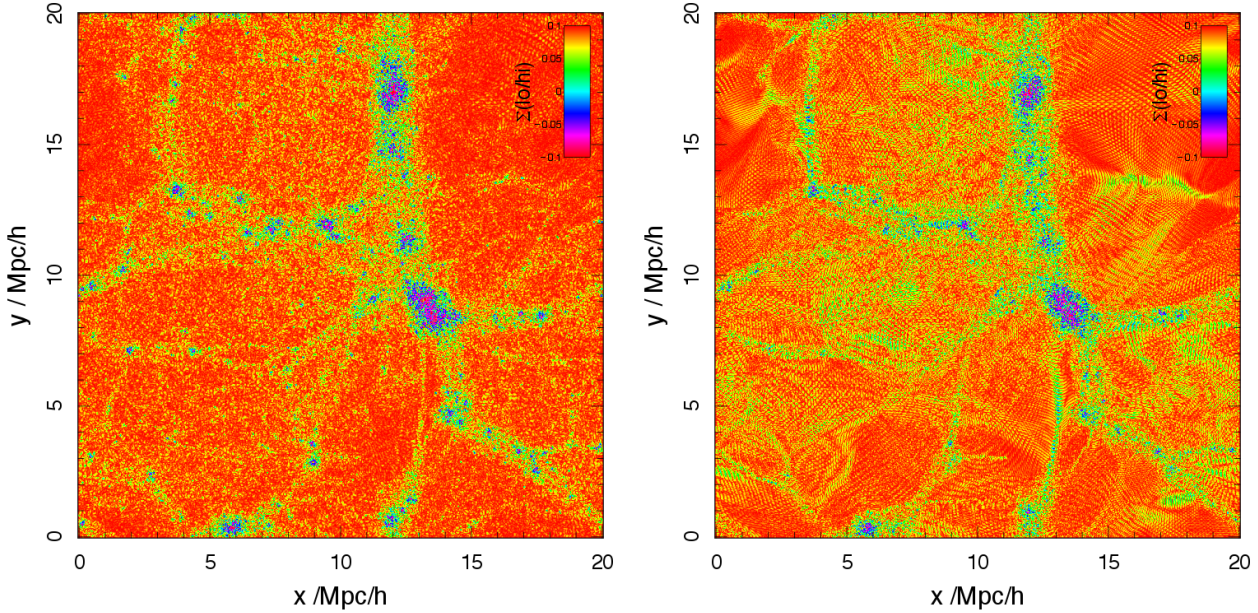


**Figure 10. Difference Maps: Delineating by Mass.** Here we show the difference in projected density between heavy and light particles in the  $\epsilon/\epsilon_0=0.01$  CDM and WDM runs (left and right panels respectively). As before, we use the atan mapping in the R `magicaxis` package.

run, where the long coherent threads of light and heavy particles, so evident in the WDM run, are fragmented, with small-scale structure present, and can be identified with the fog of lower-mass haloes mentioned previously.

In Figures 11, we investigate the consistency between simulations of differing  $\epsilon/\epsilon_0$  by cross matching FOF groups in the CDM runs (upper panel) and WDM runs (lower panel) and directly comparing particles (using GADGET2 IDs), requiring that more than 90% of particles to be in common. The heavy solid curve is the FOF group mass function measured in the  $\epsilon/\epsilon_0=0.01$  run, while the dashed, dotted, and dotted-dashed curves correspond to the mass functions of halos that are recovered in the (i)  $\epsilon/\epsilon_0=0.1$  and 0.01, (ii) 0.01 and 1, and (iii) 0.1 and 1 runs respectively. The light dashed vertical line indicates the limiting halo mass we might expect naively if the formation of structure with  $r_{200}$  smaller than  $\epsilon=\epsilon_0$  is suppressed; the limit corresponding to the  $0.1\epsilon_0$  lies off the plot. Recall that these results are for  $m_{\text{WDM}}=0.2 \text{ keV}/c^2$ , and so the appropriate half-mode mass is  $M_{\text{WDM}}^{\text{half}} \simeq 1.5 \times 10^{12} h^{-1} M_\odot$  (cf. Eq 6).

There are a number of interesting points worthy of note in these Figures. We see in the CDM runs that the mass functions turn over at lower masses, as we expect; in the  $\epsilon/\epsilon_0=0.1$  to 1 and 0.01 to 1 runs, the turn-over occurs at  $\sim 1/10^{\text{th}}$  the limit we naively expect to be imposed by softening, equivalent to a few hundred particles, and there is little difference between the two cases. In contrast, the turn-over in the  $\epsilon/\epsilon_0=0.1$  to 0.01 run becomes pronounced at  $\sim 10$  larger than the limit  $r_{200} = 0.1\epsilon_0$ , equivalent to a few tens of particles. This behaviour can be understood if one considers the WDM runs; here the turn-over in the  $\epsilon/\epsilon_0=0.1$  to 1 and 0.01 to 1 runs occurs very close to the limit imposed by softening, although there is now an upturn at lower masses. There is the hint of a turn-over in the  $\epsilon/\epsilon_0=0.1$  to 0.01 run at low masses, in agreement with the CDM run, but we find that it agrees well with the shape and amplitude of the Sheth & Tormen (1999) mass function computed with HMFCalc (Murray et al. 2013). Note also that the turn-over in

the  $\epsilon/\epsilon_0=0.1$  to 1 and 0.01 to 1 runs coincides with the upturn in the mass function that is attributed to spurious halos.

The sharp turn-over at higher masses and the upturn at lower masses evident in the  $\epsilon/\epsilon_0=0.1$  to 1 and 0.01 to 1 runs reflects the cold nature of collapse in the WDM model; the structures (typically linear) contributing to the upturn collapse relatively late compared to their CDM counterparts because of the reduced small scale power and are prevented from collapsing further because of the influence of softening, but are still sufficiently overdense to be linked together by the FOF criteria. This is not so in the CDM case; here collapse proceeds at early times anisotropically, and although softening helps to suppress smaller scale perturbations, they are still sufficient to seed collapse on mass scales below the approximate limit imposed by softening. There is no compelling physical reason why this upturn in the WDM runs should be physical, and likely reflects the difficulty the traditional  $N$ -body approach has in the limit where discreteness-driven relaxation are important.

**Halo Structure:** To complete our analysis, we follow BK02 and consider the composition of the FOF groups by computing the ratio of the numbers of low- and high-mass particles ( $N_{\text{lo}}$  and  $N_{\text{hi}}$  respectively). BK02 looked for the effects of mass segregation driven by relaxation on the internal structure of haloes; in its absence, we would expect uniformly mixed groups with  $N_{\text{lo}}/N_{\text{hi}}=1$ . In Figure 12 we compare the mean of the ratio  $N_{\text{lo}}/N_{\text{hi}}$  in each FOF group as a function of the total number of particles in the group ( $N_{\text{FOF}}$ ) for the CDM and WDM runs (upper and lower panels), in bins of 0.25 dex, for softenings between  $\epsilon/\epsilon_0=0.01$  up to an extreme of 10; this is equivalent to Figure 4 of BK02. Vertical lines indicate:

- the number of particles corresponding to the Wang & White (2007) limiting mass for spurious haloes in WDM runs (blue is for the  $64^3$  runs, for direct comparison with BK02, while red is for the  $256^3$  runs).

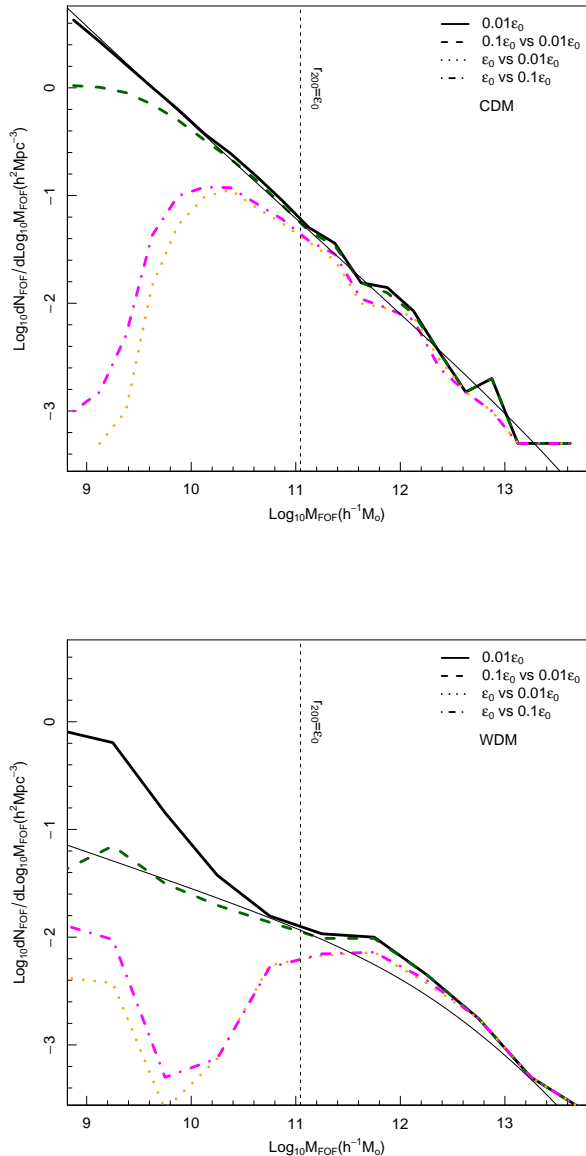


**Figure 11. Matched FOF Group Mass Functions** Here we disentangle the contributions of spurious halos to the differential mass functions of FOF groups in the CDM runs (upper panel) and WDM runs (lower panel). The dashed, dotted, and dotted-dashed curves represent the number densities of halos that have been identified in the cross-matched FOF catalogues - 0.1 to 0.01, 1 to 0.01, and 1 to 0.1  $\epsilon/\epsilon_0$ ; the heavy and light solid curves are the measured mass functions in the 0.01  $\epsilon/\epsilon_0$  runs and the predictions from Sheth & Tormen (1999). For reference, the vertical dashed line indicates the (approximate) minimum halo mass we might expect in the  $\epsilon/\epsilon_0=1$  run, where the halo virial radius  $r_{200}$  is set to  $\epsilon_0$ . Recall that for  $m_{\text{WDM}}=0.2$  keV/c<sup>2</sup>, the appropriate half-mode mass is  $M_{\text{WDM}}^{\text{half}} \simeq 1.5 \times 10^{12} h^{-1} M_\odot$ .

- the number of particles in a halo for which the relaxation time

$$t_{\text{relax}} \sim \frac{0.1}{H_0} \frac{N_{\text{FOF}}}{8 \log N_{\text{FOF}}} \quad (9)$$

is equal to the Hubble time ( $t_{\text{Hub}} \sim 1/H_0$ ) (for reference).

There are a number of interesting points worthy of note in Figure 12. First, we find trends in our CDM runs with  $\epsilon/\epsilon_0 \leqslant 0.1$  similar to those reported in BK02, who interpreted them as evidence for two-body relaxation – the ratio  $N_{\text{lo}}/N_{\text{hi}}$  is order unity for FOF groups containing  $N_{\text{FOF}} \gtrsim 1000$  particles, dips below unity for  $N_{\text{FOF}} \sim 100 - 1000$  particles, and rises sharply for  $N_{\text{FOF}} \lesssim 100$  particles. Second, softening alleviates the effects of two-body relaxation within groups – compare the solid, dotted and dashed curves; the smaller the softening, the larger the discrepancy between the measured ratio and the ideal unity. Third, softening helps suppress two-body relaxation in larger groups, but it becomes ineffective once  $N_{\text{FOF}} \lesssim 100$  particles; in larger groups, softening affects structure in the sense that  $N_{\text{lo}}/N_{\text{hi}} \lesssim 1$ , i.e. higher mass particles outnumber lower mass particles, which is what we would expect if mass segregation is occurring – the higher mass particles contribute a larger fraction of the halo mass, and so will be the dominant contribution to  $N_{\text{FOF}}$ . Below 100 particles, the ratio  $N_{\text{lo}}/N_{\text{hi}} \lesssim 1$  shows an upturn, which coincides with lower mass haloes on the outskirts of more massive haloes containing many of the low mass particles that have been displaced from the higher mass haloes through mass segregation. Fourth, the effect of too small a softening is less pronounced in WDM runs, but it is still evident. Interestingly, the Wang & White (2007) limiting mass tracks the upturn in the cross-matched mass function that we see in the WDM runs in Figure 11.

### 3.3 Summary

Taken together, these results demonstrate that discreteness-driven relaxation affects the abundance of small-scale structure in all cosmological  $N$ -body simulations. These effects are most readily apparent in WDM simulations, but we see evidence in the CDM simulations for the same process occurring; however, it is masked by the earlier onset of structure formation in CDM models on the lowest mass scales, relative to the WDM model. Use of conservative gravitational softenings  $\epsilon = \bar{d}$  can help suppress the formation of unphysical small-scale structure, at the expense of the internal structure of haloes, but it cannot wholly eliminate it. This provides additional motivation for new approaches (e.g. Hahn et al. 2013; Angulo et al. 2013b; Hahn & Angulo 2016; Hobbs et al. 2015).

## 4 CONCLUSIONS

We have explored the influence of discreteness-driven relaxation in cosmological  $N$ -body simulations. Our motivation for doing this was to understand what role such relaxation might play in the formation of spurious haloes, most readily apparent in WDM simulations. We reasoned that the early stages of gravitational collapse, which proceeds in an anisotropic fashion as regions are sheared out into sheets and filaments (cf. Kuhlman, Melott, & Shandarin 1996), is susceptible to errors arising from discreteness effects because particles move in a smooth mean-field gravitational potential modified by localised perturbations, i.e. other particles. Encounters with these perturbations modify the momentum distribution of particles and can seed the formation of unphysical structures.

Using an idealised model for anisotropic collapse, the plane-symmetric collapse test as set out in Zel'dovich (1970) and Shandarin & Zeldovich (1989), we demonstrated this effect, showing that close encounters at shell crossing seeds the formation of unphysical clumpy structures at later times, regularly spaced at intervals of the mean inter-particle separation  $\bar{d}$ , which scales naturally

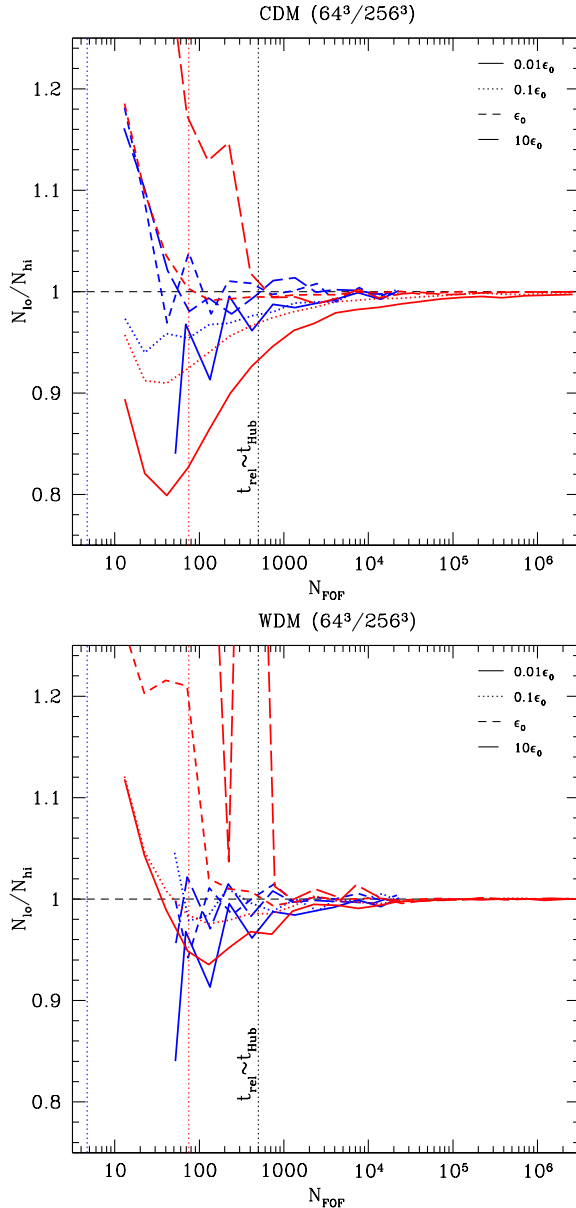


**Figure 12. Evidence for Two-Body Relaxation in CDM and WDM Runs.** Following Binney & Knebe (2002), we use the ratio of the numbers of low-to-high resolution particles (i.e. the numbers of heavy-to-light particles) to measure the influence of two-body relaxation on the formation of haloes containing few particles. Solid, dotted, short- and long-dashed curves represent the  $\epsilon/\epsilon_0=0.01, 0.1, 1$  and  $10$  CDM and WDM  $1/4$  runs (upper and lower panels); curves coloured red and blue correspond to runs with  $2 \times 64^3$  and  $2 \times 256^3$  particles. The rightmost dotted vertical line indicates the size of FOF group ( $N_{\text{FOF}}$ ) below which the relaxation time is shorter than the Hubble time; the red and blue dotted vertical lines indicate the value of  $N_{\text{FOF}}$  above which the Wang & White (2007) criterion is satisfied.

as  $m_p^{1/3}$ . We showed also that this effect depends on the magnitude of the kernel spline gravitational softening scale  $\epsilon$ , and adopting  $\epsilon \sim \bar{d} = \epsilon_0$  can suppress the effect. These effects were particularly striking when we modelled the mass distribution using two collisionless components, in which we varied the mass ratio between  $1/1$  to  $1/10$  and softenings between  $\epsilon/\epsilon_0=(1,0.1,0.01)$ , such that

the larger the mass ratio and the smaller the softening, the larger the perturbation at shell crossing.

We applied these insights to cosmological  $N$ -body simulations consisting of two collisionless components of differing fixed masses ( $1/\sqrt{2}$  and  $1/4$  respectively), designed to highlight the effect of discreteness-driven relaxation, and found evidence for the effects that we observed in plane-symmetric collapse simulations. These effects were most evident in the WDM simulations, in the characteristic beads-on-a-string structures within filaments and in the upturn of the FOF group mass function, but they were also present in the CDM runs, most notably in the spatial distribution of low-mass groups in low-density regions – the so-called fog – in runs with  $\epsilon/\epsilon_0 < 1$ , where we defined  $\epsilon_0 = \bar{d}$ . We found that choosing softenings  $\epsilon/\epsilon_0=1$  could suppress the effects of relaxation, but could not wholly eliminate them in realistic circumstances. In the case of WDM runs, the dearth of small-scale power that is present in CDM means that these effects will be most apparent when collapse first becomes non-linear at relatively late times, in larger-scale filaments; the momentum distribution of particles is unaffected until then. In contrast, small-scale power drives collapse early in CDM runs and so the momentum distribution of particles is modified at early times; perturbations act to scatter momenta isotropically and this is imprinted on the momentum distribution we would expect from linear perturbation theory. In runs with small softenings, these momentum perturbations are larger and give rise to the fog of low-mass groups evident in Figure 6.

In other words, the spurious halo problem is a generic one, affecting the CDM model and its WDM and WDM-like counterparts alike. This is consistent with the earlier work of Ludlow & Porciani (2011), who noted a “missing progenitor” problem in  $N$ -body simulations of the CDM model, and with Melott et al. (1997) and Heitmann et al. (2005), who found that codes in which the gravitational force between particles is softened are unable to recover the analytical solution if the softening scale is smaller than the mean inter-particle separation, which Melott et al. (1997) argued represented collisionality. This is because the fundamental assumption underlying  $N$ -body simulations – that the system is collisionless and integration of the equations of motion provides a solution to the Vlasov equation – ultimately falters because  $N$  is finite, which implies that discreteness effects will play a role in the evolution of the system. This is leading to the development of new algorithms, such as approaches to solve dark matter dynamics in phase space (cf. Hahn et al. 2013; Sousbie & Colombi 2015; Hahn & Angulo 2016), and revisions of the traditional  $N$ -body approach, such as spatially adaptive (e.g. Iannuzzi & Dolag 2011; Hobbs et al. 2015) and anisotropic gravitational softenings.

This has important implications for predictions of cosmological structure formation and galaxy formation derived from traditional  $N$ -body simulations. If discreteness-driven relaxation seeds spurious halo formation, we might expect that the initial phases of halo formation will tend to occur prematurely<sup>3</sup> impact halo struc-

<sup>3</sup> This may be a naive expectation. For example, it may be more correct to say that it introduces a scatter between the predicted and numerically recovered anisotropic collapse times; depending on the details of collapse, these times may earlier or later than expected. It is also interesting to note that these may have consequences at late times. Previous studies (e.g. van den Bosch 2002; Giocoli et al. 2007; Power et al. 2012), which compare the formation times of simulated halos and the predictions of extended Press-Schechter (EPS) theory, report that the formation times of simulated halos are systematically earlier than (EPS) predictions.

ture at later times, allowing for the influence of merger history. This is because overly dense progenitors sink to the centre as they merge to form more massive systems, and will artificially enhance central density (see also Binney & Knebe 2002). This is likely to lead to a modification of the well studied relationship between halo mass and concentration (cf. Navarro, Frenk, & White 1997; Bullock et al. 2001; Duffy et al. 2008; Dutton & Macciò 2014; Ludlow et al. 2014; Correa et al. 2015) at lower masses – the influence should be erased at higher masses through the effects of repeated merging – and suggests that the disparity reported in the slope at lower masses of relations proposed by different authors (see discussion in Correa et al. 2015) could be numerically driven. This also implies that low-mass haloes accreted later could survive for longer because of their enhanced central densities, possibly giving rise to many more substructures than we might otherwise expect, although it is worth nothing that these are also the systems whose central structure is most poorly resolved and so are subject to enhanced numerically-driven tidal disruption.

In addition, the combination of earlier formation times and enhanced survival during merging will influence the predictions of galaxy formation models based on the semi-analytical approach coupled to  $N$ -body merger trees (cf. Baugh 2006) – haloes can form stars earlier, and more of these haloes containing stars will survive to merge with central galaxies. This will have consequences for the predicted luminosity function and the calibration of different modes of feedback, including active galactic nuclei the most massive dark matter halos. Of course, the impact of this effect can be gauged by means of Monte Carlo merger trees based on extended Press-Schechter theory (e.g. Parkinson et al. 2008).

It also affects hydrodynamical simulations, where it is standard practice in smoothed particle hydrodynamics (SPH) runs to use equal numbers of gas and dark matter particles, which for typical cosmological simulations leads to a mass ratio of  $\Omega_b/(\Omega_0 - \Omega_b) \simeq 1/6$  between them, where  $\Omega_b$  is the baryon density parameter; when coupled to small gravitational softenings, this can lead to both spurious heating (as has been known for some time; see, e.g. Steinmetz & White 1997) as well as spurious growth (cf. O’Leary & McQuinn 2012, Angulo et al. 2013a).

We have outlined a number of important consequences of the effects of discreteness-driven relaxation for predictions of cosmological structure formation and galaxy formation. Broadbrush predictions will be unaffected – for example, there are sound theoretical reasons to expect cuspy dark matter halos (e.g. Moore 1994; Schulz et al. 2013) – but the devil will be in the detail – for example, what is the true predicted abundance of CDM dark matter subhalos around a galaxy like the Milky Way, and how should we expect the internal structure of subhalos to be affected? These are strong arguments for a more considered approach to the limitations of  $N$ -body simulations, powerful a tool as they may be, and provides additional motivation for the need of new approaches (e.g. Hahn & Angulo 2016; Hobbs et al. 2015; Soubie & Colombi 2015).

## ACKNOWLEDGMENTS

The authors are indebted to the referee whose careful reading of the paper and their insightful suggestions have helped to improve it. CP, GFL and DO acknowledge support of Australian Research Council (ARC) DP130100117. CP, ASGR, GFL and DO acknowledge support of ARC DP140100198. CP acknowledges support of ARC FT130100041. All simulations presented in this paper were carried out using computational resources on the Magnus super-

computer at the Pawsey Supercomputing Centre through the National Computational Infrastructure Merit Allocation Scheme. The research presented in this paper is undertaken as part of the Survey Simulation Pipeline (SSimPL; <http://ssimpl.org/>).

This paper has been typeset from a  $\text{\TeX}$  /  $\text{\LaTeX}$  file prepared by the author.

## REFERENCES

- Angulo, R. E., Hahn, O., & Abel, T. 2013a, MNRAS, 434, 1756
- Angulo R. E., Hahn O., Abel T., 2013b, MNRAS, 434, 3337
- Athanassoula E., Fady E., Lambert J. C. & Bosma A., 2000, MNRAS, 314, 475
- Baugh, C. M. 2006, Reports on Progress in Physics, 69, 3101
- Bagla J. S., Prasad J., 2009, MNRAS, 393, 607
- Bardeen, J. M., Bond, J. R., Kaiser, N., & Szalay, A. S. 1986, ApJ, 304, 15
- Benson, A. J., Farahi, A., Cole, S., et al. 2013, MNRAS, 428, 1774
- Bergström, L. 2000, Reports of Progress in Physics, 63, 793
- Binney, J., & Knebe, A. 2002, MNRAS, 333, 378
- Binney J., 2004, MNRAS, 350, 939
- Binney, J., & Tremaine, S. 2008, Galactic Dynamics: Second Edition, by James Binney and Scott Tremaine. ISBN 978-0-691-13026-2 (HB). Published by Princeton University Press, Princeton, NJ USA, 2008..
- Bird S., Viel M., Haehnelt M. G., 2012, MNRAS, 420, 2551
- Bode, P., Ostriker, J. P., & Turok, N. 2001, ApJ, 556, 93
- Bullock J. S., Kolatt T. S., Sigad Y., Somerville R. S., Kravtsov A. V., Klypin A. A., Primack J. R., Dekel A., 2001, MNRAS, 321, 559
- Colín, P., Valenzuela, O., & Avila-Reese, V. 2008, ApJ, 673, 203
- Correa, C. A., Wyithe, J. S. B., Schaye, J., & Duffy, A. R. 2015, MNRAS, 452, 1217
- Diemand J., Moore B., Stadel J. & Kazantzidis S., 2004, MNRAS, 348, 977
- Duffy A. R., Schaye J., Kay S. T., Dalla Vecchia C., 2008, MNRAS, 390, L64
- Dutton A. A., Macciò A. V., 2014, MNRAS, 441, 3359
- El-Zant A. A., 2006, MNRAS, 370, 1247
- Giocoli C., Moreno J., Sheth R. K., Tormen G., 2007, MNRAS, 376, 977
- Green, A. M., Hofmann, S., & Schwarz, D. J. 2004, MNRAS, 353, L23
- Abel T., Hahn O., Kaehler R., 2012, MNRAS, 427, 61
- Hahn, O., Abel, T., & Kaehler, R. 2013, MNRAS, 434, 1171
- Hahn, O., & Paranjape, A. 2014, MNRAS, 438, 878
- Hahn O., 2014, Proceedings of IAU Symposium 308 “The Zeldovich Universe: Genesis and Growth of the Cosmic Web”, 23–28 June 2014, Tallinn, Estonia (arXiv:1412.5197)
- Hahn O., Angulo R. E., 2016, MNRAS, 455, 1115
- Heitmann K., Ricker P. M., Warren M. S., Habib S., 2005, ApJS, 160, 28
- Hernquist L. & Barnes J. E., 1990, ApJ, 349, 562
- Hobbs A., Read J., Agertz O., Iannuzzi F., & Power C., 2016, MNRAS, 458, 468
- Iannuzzi F., & Dolag K., 2011, MNRAS, 417, 2846
- Ishiyama, T., Rieder, S., Makino, J., et al. 2013, ApJ, 767, 146

- Jenkins, A., Frenk, C. S., White, S. D. M., et al. 2001, MNRAS, 321, 372
- Klypin, A., Holtzman, J., Primack, J., & Regos, E. 1993, ApJ, 416, 1
- Komatsu, E., Smith, K. M., Dunkley, J., et al. 2011, ApJS, 192, 18
- Knebe A., Kravtsov A. V., Gottlöber S., Klypin A. A., 2000, MNRAS, 317, 630
- Knebe A., Devriendt J. E. G., Mahmood A., Silk J., 2002, MNRAS, 329, 813
- Knebe A., Devriendt J. E. G., Gibson B. K., Silk J., 2003, MNRAS, 345, 1285
- Kuhlman B., Melott A. L., Shandarin S. F., 1996, ApJ, 470, L41
- Lewis, A., Challinor, A., & Lasenby, A. 2000, ApJ, 538, 473
- Loeb, A. & Weiner, N. 2011, Physical Review Letters, 106, 171302
- Lovell M. R., et al., 2012, MNRAS, 420, 2318
- Lovell M. R., Frenk C. S., Eke V. R., Jenkins A., Gao L., Theuns T., 2014, MNRAS, 439, 300
- Ludlow, A. D., & Porciani, C. 2011, MNRAS, 413, 1961
- Ludlow A. D., Navarro J. F., Angulo R. E., Boylan-Kolchin M., Springel V., Frenk C., White S. D. M., 2014, MNRAS, 441, 378
- Macciò A. V., Paduroiu S., Anderhalden D., Schneider A., Moore B., 2012, MNRAS, 424, 1105
- Macciò A. V., Ruchayskiy O., Boyarsky A., Muñoz-Cuartas J. C., 2013, MNRAS, 428, 882
- Melott, A. L., Shandarin, S. F., Splinter, R. J., & Suto, Y. 1997, ApJL, 479, L79
- Moore, B. 1994, Nature, 370, 629
- Moore, B., Quinn, T., Governato, F., Stadel, J., & Lake, G. 1999, MNRAS, 310, 1147
- Murray, S. G., Power, C., & Robotham, A. S. G. 2013, Astronomy and Computing, 3, 23
- Myers, A., Colella, P., & Van Straalen, B. 2015, arXiv:1503.05969
- Navarro J. F., Frenk C. S., White S. D. M., 1997, ApJ, 490, 493
- Navarro, J. F., Ludlow, A., Springel, V., et al. 2010, MNRAS, 402, 21
- O’Leary, R. M., & McQuinn, M. 2012, ApJ, 760, 4
- Pacucci, F., Mesinger, A., & Haiman, Z. 2013, MNRAS, 435, L53
- Parkinson, H., Cole, S., & Helly, J. 2008, MNRAS, 383, 557
- Power, C., Navarro, J. F., Jenkins, A., et al. 2003, MNRAS, 338, 14
- Power, C., Knebe, A., & Knollmann, S. R. 2012, MNRAS, 419, 1576
- Power, C. 2013, PASA, 30, 53
- Romeo A. B., Agertz O., Moore B., Stadel J., 2008, ApJ, 686, 1
- Schneider A., Smith R. E., Macciò A. V., Moore B., 2012, MNRAS, 424, 684
- Schneider, A., Smith, R. E., & Reed, D. 2013, MNRAS, 433, 1573
- Schulz, A. E., Dehnen, W., Jungman, G., & Tremaine, S. 2013, MNRAS, 431, 49
- Shandarin S. F., Zeldovich Y. B., 1989, RvMP, 61, 185
- Sheth, R. K., & Tormen, G. 1999, MNRAS, 308, 119
- Smith, R. E. & Markovic, K. 2011, Phys. Rev. D, 84, 063507
- Sousbie, T., & Colombi, S. 2015, arXiv:1509.07720
- Splinter R. J., Melott A. L., Shandarin S. F., Suto Y., 1998, ApJ, 497, 38
- Springel, V., White, S. D. M., Tormen, G., & Kauffmann, G. 2001, MNRAS, 328, 726
- Springel, V. 2005, MNRAS, 364, 1105
- Springel, V., Frenk, C. S., & White, S. D. M. 2006, Nature, 440, 1137
- Springel, V., Wang, J., Vogelsberger, M., et al. 2008, MNRAS, 391, 1685
- Steinmetz, M., & White, S. D. M. 1997, MNRAS, 288, 545
- Thiébaut J., Pichon C., Sousbie T., Prunet S. & Pogosyan D., 2008, MNRAS, 387, 397
- Valageas P., 2012, PhRvD, 86, 123501
- van den Bosch F. C., 2002, MNRAS, 331, 98
- Viel M., Haehnelt M. G., Springel V., 2010, JCAP, 6, 15
- Viel M., Marković K., Baldi M., Weller J., 2012, MNRAS, 421, 50
- Vogelsberger M., Zavala J., Loeb A., 2012, MNRAS, 423, 3740
- Wang, J., & White, S. D. M. 2007, MNRAS, 380, 93
- Watson, W. A., Iliev, I. T., D’Aloisio, A., et al. 2013, MNRAS, 433, 1230
- Yoshida, N., Sugiyama, N., & Hernquist, L. 2003, MNRAS, 344, 481
- Zel’dovich Y. B., 1970, A&A, 5, 84

## APPENDIX A: INFLUENCE OF TREEPM ALGORITHM

We have demonstrated in § 3.1 that particle discreteness introduces gravitational perturbations when the gravitational softening length is smaller than the mean inter-particle separation, which breaks the symmetry inherent in the plane-symmetric collapse problem and seeds the formation of spurious structures. This will be sensitive to both the manner and the accuracy with which we calculate forces, the errors in which can be asymmetric and which can in turn seed perturbations that form spurious structures. This is especially true in the case of pure Tree codes, where force errors are non-Cartesian. We have tested the sensitivity of our results to the TreePM algorithm used in GADGET2 by running a subset of our simulations using a purely Tree calculation (hereafter NoPM) as well as the default hybrid TreePM calculation with increasing PM dimension, from  $N_{\text{mesh}}=64$  to 1024 in factors of 2 (hereafter PM- $N_{\text{mesh}}$ ). Recall that we have used by default the TreePM option with a PM dimension of 512.

**Plane-Symmetric Collapse:** Here we assess how the  $256^3$  version of the plane-symmetric collapse problem, with  $\epsilon/\epsilon_0=0.1$ , is affected by influenced by our choice of PM dimension by looking at the phase space structure at  $z=0$  in Figure A1 and the corresponding projected spatial structure in Figure A2. From top left to bottom right, we show results for the NoPM, PM-128, PM-256, and PM-512 runs; variations in CPU time per run were less than  $\sim 3\%$ .

The clumping seeded at shell crossing that is evident in Figure 2 is also apparent in Figure A1, independent of our choice of PM dimension, although the degree of clumping reduces as PM dimension increases. A similar trend is evident in Figure A2. These results suggest that the greater force asymmetries and inaccuracies implicit in runs with coarser PM dimension amplify, rather than give rise to, the discreteness-driven relaxation effects that we report.

**Cosmological Simulations:** We now consider the CDM version of the two collisionless component run with mass ratio of 1/4 and  $\epsilon/\epsilon_0=0.1$ , with a focus on the power spectrum of density perturbations and on the abundance of FOF groups at  $z=0$ .

A few key diagnostics of the runs are presented in Table A1.

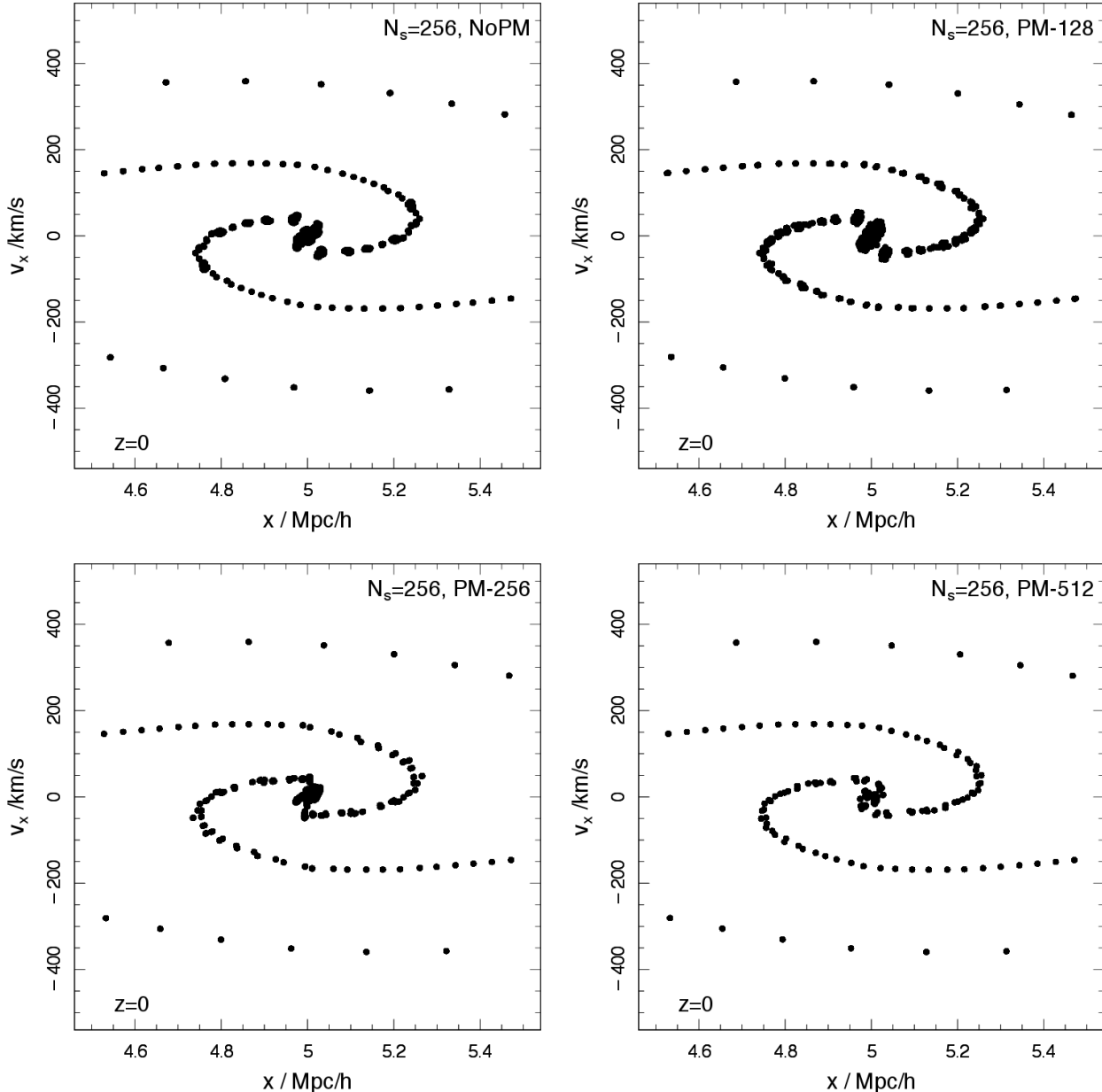


**Figure A1. Plane-Symmetric Collapse: Phase Space Structure.** Here we show how the phase space structure in the  $256^3$  run at approximately shell crossing ( $z \simeq 4$ ) is affected by the PM dimension of the TreePM algorithm. As in Figure 2,  $v_x$  is the peculiar velocity along the  $x$ -direction and  $x$  is the comoving position. The gravitational softening  $\epsilon = 0.1\epsilon_0$ .

For the given problem size, the PM-512 calculation is most computationally efficient, while neglecting the PM component completely results in a calculation that is half as efficient. There is little variation in the numbers of FOF groups with in excess of 1000 particles that form, as we would expect; their formation is driven by the large scale gravitational field, and although their evolution in detail may be affected by force inaccuracies, these will not be sufficient to significantly affect which regions collapse and what masses they reach. In contrast, there is a trend for the numbers of FOF groups with in excess of 10 and 100 particles to decrease as finer TreePM calculations are used, with the PM cell dimension matching the mean inter-particle separation as the transition point (i.e.  $N_{\text{mesh}}=256$ ).

In Figure A3 we show how the measured power spectra at  $z=0$

are affected by force errors by plotting the power spectra  $P(k)$  between  $k_{\min} = 2\pi/L_{\text{box}} \simeq 0.3h \text{ Mpc}^{-1}$  and  $k_{\max} = k_{\text{Nyquist}} = \pi N_{\text{mesh}}/L_{\text{box}} \simeq 3.1 \times 10^{-4}h \text{ Mpc}^{-1}$ , normalised to the power spectrum measured in the PM-1024 calculation,  $P(k)^{1024}$ . Here  $k_{\text{Ny}}$  is the Nyquist frequency of the FFT mesh - of dimension 512 - used to calculate the power spectrum, and we have used the Cloud-in-Cell mass assignment scheme when computing overdensities. Dashed horizontal lines indicate a ratio of unity and 10%, while the heavy solid, shorted dashed, dotted, dotted-dashed, and long dashed curves correspond to the ratios obtained for the NoPM, PM-64, PM-128, PM-256, and PM-512 runs respectively. The NoPM run shows the largest deviation, in excess of 10% at  $k \simeq 10h \text{ Mpc}^{-1}$ , which is approximately the inverse mean inter-particle separation

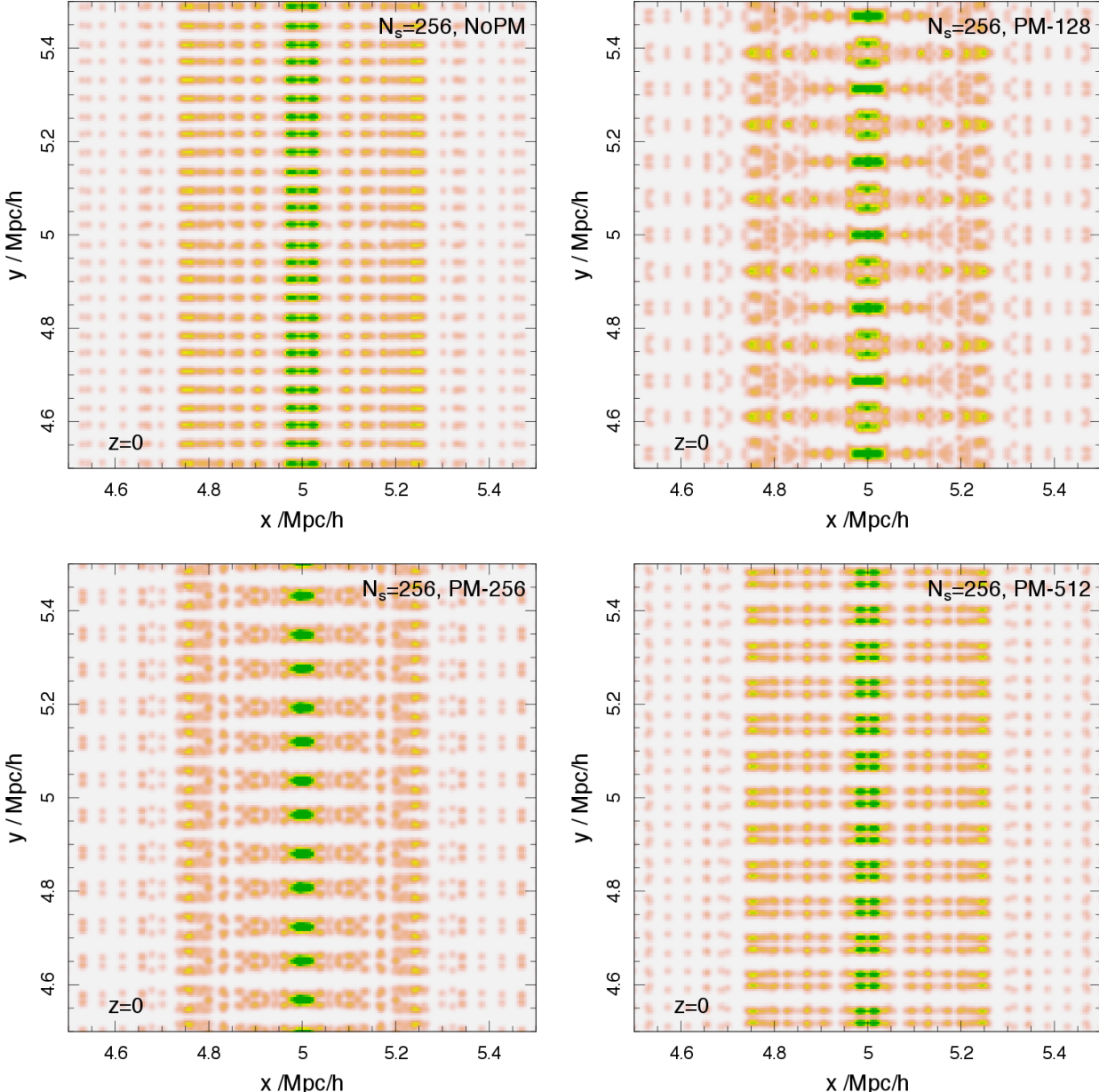


**Figure A2. Plane-Symmetric Collapse: Spatial Structure.** Here we show how the projected spatial distribution (in the  $x$ - $y$  plane) at  $z=0$  in the  $256^3$  run is affected by the PM dimension of the TreePM algorithm. Positions are in comoving coordinates, while the gravitational softening  $\epsilon=0.1\epsilon_0$ .

of the simulation; otherwise the TreePM runs show progressively smaller deviations with respect to the PM-1024 run from PM-64 to PM-128 to PM-256, at which point there is little difference between the PM-256 and PM-512 results. All of the runs show an excess at high wavenumber, approximately at the scale of the inverse of the comoving softening.

In Figure A4, we show how the FOF group mass functions at  $z=0$  are affected by the PM dimension by comparing the abundance of halos cross matched with respect to the PM-1024 run to the abundance of all halos in the PM-1024 run. The mass functions are consistent down to a mass of  $\sim 10^{10.5} h^{-1} M_\odot$ , which is equivalent to  $\sim 1000$  particles, before declining sharply such that the deviation exceeds  $\sim 10\%$  at  $\sim 10^{9.5} h^{-1} M_\odot$ , which is equivalent to  $\sim 100$  particles. These trends are in excellent agreement between runs,

and, as we have concluded above, this implies that force asymmetries and inaccuracies amplify rather than give rise to the effects of discreteness-driven relaxation.

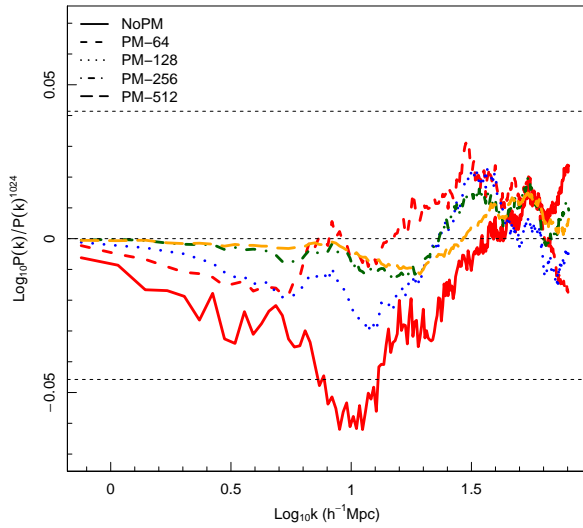


**Figure A3. Impact on Power Spectrum:** Here we plot the power spectrum normalised to the power spectrum measured in the PM-1024 run; solid, dashed, dotted, dotted-dashed, and long dashed curves correspond to the NoPM, PM-64, PM-128, PM-256, and PM-512 runs respectively. Dashed horizontal lines indicate unity and deviations of  $\pm 10\%$ .

**Table A1. Sensitivity to TreePM Algorithm:** Here  $N$  is the PM dimension along 1 dimension;  $f_{\text{CPU}}$  is the CPU time in units of the time taken for the PM-1024 run; and  $N_{\text{FOF}}^{>x}$  is the number of FOF groups obtained with Sub-Find with a linking length of  $0.2 \bar{d}$  with in excess of  $x = (10, 100, 1000)$  particles. For reference, all simulations were run on 16 processors; the PM-1024 run, which took  $\sim 186$  CPU hrs.

	$N_{\text{PM}}$	$f_{\text{CPU}}$	$N_{\text{FOF}}^{>10}$	$N_{\text{FOF}}^{>100}$	$N_{\text{FOF}}^{>1000}$
NoPM	-	1.83	93282	8709	1223
PM-64	64	1.16	93702	8842	1251
PM-128	128	0.97	93806	8846	1235
PM-256	256	0.84	93508	8688	1220
PM-512	512	0.79	92384	8590	1229
PM-1024	1024	1.	91632	8568	1232

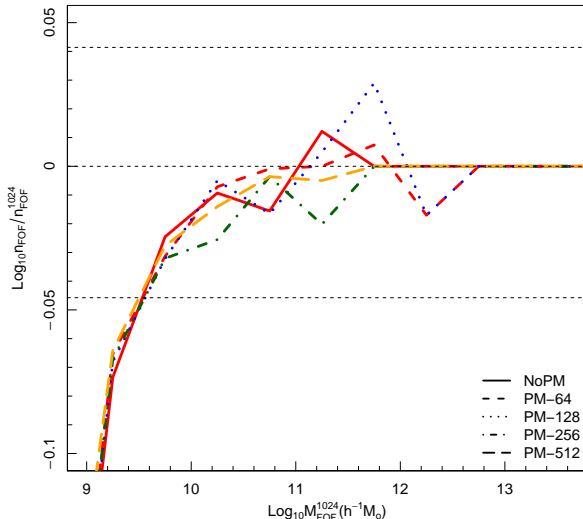


**Figure A4. Impact on FOF Group Mass Function:** Here we plot the abundance of FOF groups (for a linking length of  $0.2 \bar{d}$ ) relative to that measured in the PM-1024 run; solid, dashed, dotted, dotted-dashed, and long dashed curves correspond to the NoPM, PM-64, PM-128, PM-256, and PM-512 runs respectively. Dashed horizontal lines indicate unity and deviations of  $\pm 10\%$ .